T cells Instruct Immune Checkpoint Inhibitor Therapy Resistance in Tumors Responsive to IL-1 and TNFα Inflammation.

Nam Woo Cho[1,2], Sophia M. Guldberg[2,3], Barzin Y. Nabet[4], Jie Zeng Yu[5], Eun Ji Kim[6], Kamir J. Hiam-Galvez[2,3], Jacqueline L. Yee[2,3], Rachel DeBarge[2,3], Iliana Tenvooren[2], Naa Asheley Ashitey[2], Filipa Lynce[7], Deborah A. Dillon[8], Jennifer M. Rosenbluth[9], Matthew H. Spitzer[2]

[1]Department of Radiation Oncology, University of California, San Francisco, San Francisco, CA, USA

[2]Departments of Otolaryngology and Microbiology & Immunology, Helen Diller Family Comprehensive Cancer Center, Parker Institute for Cancer Immunotherapy, Chan Zuckerberg Biohub, University of California, San Francisco, San Francisco, CA, USA

[3]Graduate Program in Biomedical Sciences, University of California, San Francisco, San Francisco, CA, USA

[4]Stanford Cancer Institute, Stanford University, Stanford, CA, USA *present address: Genentech Inc., South San Francisco, CA, USA

[5]Department of Medicine, Division of Hematology/Oncology, University of California, San Francisco, San Francisco, CA, USA

[6]Independent researcher

[7]Dana-Farber Cancer Institute, Boston, MA, USA

[8]Department of Pathology, Brigham & Women's Hospital, Boston, MA, USA

[9]Department of Medicine, Division of Hematology/Oncology, University of California, San Francisco, and Chan Zuckerberg Biohub, San Francisco, CA, USA

Running Title: T cells instruct inflammatory immunotherapy resistance.

Corresponding authors:

Matthew H. Spitzer

UCSF Box 0552, 513 Parnassus Ave., San Francisco, CA 94143, USA

Tel: 415-476-7972

27 Email: Matthew.Spitzer@ucsf.edu

28

29 Nam Woo Cho

30 2340 Sutter St., San Francisco, CA 94115, USA

31 Email: namwoo.cho@ucsf.edu

32

33 **Conflict of Interest Statement**

34 M.H.S. is founder and shareholder of Teiko.bio and Prox Biosciences, has received a speaking honorarium from
35 Fluidigm Inc., Kumquat Bio, and Arsenal Bio, has been a paid consultant for Five Prime, Ono, January, Earli,
36 Astellas, and Indaptus, and has received research funding from Roche/Genentech, Pfizer, Valitor, and Bristol
37 Myers Squibb. E.J.K. is an employee of Thermo Fisher Scientific, and is a spouse of N.W.C.

38

39 **Abstract**

40 Resistance to immune checkpoint inhibitors (ICIs) is common, even in tumors with T cell infiltration. We
41 thus investigated consequences of ICI-induced T cell infiltration in the microenvironment of resistant tumors. T
42 cells increased in ICI-resistant tumors following treatment as did neutrophils, in contrast to ICI-responsive tumors.
43 Resistant tumors were distinguished by high expression of IL-1 Receptor 1 (IL1R1), enabling a synergistic
44 response to IL-1 and TNFα to induce G-CSF, CXCL1, and CXCL2 via NF-κB signaling, supporting neutrophils.
45 Perturbation of this inflammatory resistance circuit sensitized tumors to ICIs. Paradoxically, T cells drove this
46 resistance circuit via TNFα both *in vitro* and *in vivo*. Evidence of this inflammatory resistance circuit and its
47 impact also translated to human cancers. These data support a novel mechanism of ICI resistance, wherein
48 treatment-induced T cell activity can drive resistance in tumors responsive to IL-1 and TNFα, with important
49 therapeutic implications.

50 **Statement of Significance**

Although T cell-infiltrated cancers are frequently resistant to immune checkpoint inhibitor therapies, mechanisms of resistance beyond T cell exhaustion remain unclear. Here, we reveal the functional significance of tumor-infiltrating T cells in resistant tumors, which surprisingly instruct immunosuppressive inflammation in mouse and human cancers responsive to IL-1 and TNFα.

Introduction

Immune checkpoint inhibitors (ICIs) are integral to the armamentarium against cancer. However, these therapies are not effective in many patients, and an important mission is to better define principles determining treatment response versus failure[1]. Among core immunologic programs governing the response to ICIs is the infiltration of T cells in the tumor microenvironment (TME)[2–5], where "inflamed" or "hot" tumors, such as those with microsatellite instability-high (MSI-H) status, exhibit higher response rates to further immune activating therapies[6–10]. Nevertheless, treatment resistance to ICIs occurs commonly even in T cell-infiltrated tumors[11,12], but there is a limited understanding of how such T cell-infiltrated tumors can escape T cell-activating therapies. For example, MSI-H tumors demonstrate increased tumor neoantigen load and T cell infiltration, yet not all respond to ICIs[9–11,13–18]. We reasoned that the development of T cell infiltrated tumor models would enable study of T cell states and their interactions with the TME during ICI resistance despite T cell inflammation.

Inflammation is a broad term encompassing multiple processes that can promote or prevent tumor progression[19]. For instance, inflammation can be driven by the transcription factor nuclear factor-κB (NF-κB), which is activated in multiple cell types in the TME by various stimuli, including the cytokines TNFα and IL-1[20,21]. This circuit can drive diverse tumor promoting mechanisms including immunosuppression[22–26]. Among many known roles, NF-κB signaling can foster recruitment and activation of immunosuppressive myeloid cells to suppress T cell cytotoxicity[27–31]. Accordingly, its inhibition in the TME can lead to improved immunologic control of tumors[31–36]. Of note, T cells and NF-κB-mediated immunosuppressive inflammation can co-exist in the TME, yet their relationship is incompletely defined. Much of the recent research efforts have focused on the biology of tumor infiltrating lymphocytes (TILs), which lose stemness and differentiate toward exhaustion as a result of chronic antigen stimulation and immunosuppressive signals, including those provided by myeloid cell

77 subsets[37,38]. However, it is currently unclear whether and how conventional CD4 or CD8 T cells themselves
78 regulate inflammation in the TME, and whether the interplay between these factors shapes the immunologic
79 setpoint to affect responsiveness to immunotherapy.

80 Here, we use T cell-infiltrated mouse syngeneic tumor models of ICI response and resistance to discover
81 that T cells can drive a TNFα and IL-1-mediated inflammatory response from IL1R1-expressing tumor cells in
82 the setting of ICI resistance. TNFα and IL-1 synergistically upregulate NF-κB-transcribed cytokines including
83 G-CSF, CXCL1, and CXCL2, resulting in recruitment of immunosuppressive neutrophils to the TME.
84 Importantly, we show that this inflammatory resistance circuit requires T cells. Activated tumor-infiltrating T
85 cells were sufficient to increase G-CSF production by tumor cells *in vitro* in a TNFα-dependent manner. *In vivo,*
86 ICIs increased infiltration of TNFα-producing T cells. Breaking this inflammatory circuit via pharmacologic or
87 genetic perturbation of IL1R1 or TNFα, including tumor cell-specific deletion of IL1R1 or T cell-specific deletion
88 of TNFα, sensitized resistant tumors to ICIs. Finally, analyses of human datasets corroborate these cellular and
89 mechanistic elements in patients treated with ICIs, revealing correlation of ICI-induced infiltration of *TNF*+ T
90 cells and NF-κB activity in IL1R1-expressing tumors, as well as the adverse impact of the inflammatory resistance
91 axis on ICI treatment outcome. These findings refine the current paradigm of T cell responses to ICI therapy with
92 significant clinical implications, revealing an opportunity to dissociate the tumor-promoting aspects of T cell
93 activity from their tumoricidal functions to improve therapeutic benefit.

94

95 **Results**

96 <u>T Cell-Infiltrated Mouse Syngeneic Tumors Demonstrate Variable Responses to ICIs</u>

97 Tumors lacking T cell infiltration are generally resistant to ICIs. While the opposite may be expected for
98 tumors with high T cell infiltration, a significant fraction nevertheless demonstrates treatment resistance[11,12]. To
99 understand mechanisms of ICI response and resistance in T cell-infiltrated tumors, we generated mouse syngeneic
100 tumor cell lines lacking the DNA mismatch repair protein, MSH2, to create microsatellite instability-high (MSI-
101 H) cells. While the response rates to ICIs are generally favorable, treatment resistance is nevertheless frequently

102 seen in patients with response rates ranging from 30-50% in pre-treated settings[11,17,18], and in mouse MSI-H tumor
103 models[39,40]. Thus, we utilized this opportunity to study ICI response and resistance in the context of T cell
104 infiltration. *Msh2* gene deletion by CRISPR-Cas9 ribonucleoprotein electroporation[41] in the polyclonal cell pool
105 almost completely abolished MSH2 protein expression, eliminating the requirement for single cell cloning and
106 allowing preservation of any parental tumor heterogeneity, which has been shown to impact immunogenicity and
107 ICI sensitivity[42] (Fig. 1A and B; Supplementary Fig. S1A; Supplementary Table S1). Cell lines generated in this
108 manner accumulated microsatellite instability assessed by PCR[9,43] over 4 months, or 60 passages, of continuous
109 culture (Fig. 1C; Supplementary Fig. S1B; Supplementary Table S2). Compared to control microsatellite-stable
110 (MSS) cell lines generated using nontargeting guide RNA and cultured for the same duration, the MSI-H cell
111 lines accumulated single nucleotide polymorphisms and indels when quantified by whole exome sequencing (Fig.
112 1D). These data are consistent with the level of MSI reported in published mouse studies[9,10]. Each tumor cell line
113 transcribed neoantigens with a similar distribution and heterogeneity of predicted antigenicity and allele
114 frequency, calculated using MuPeXI with inputs including neopeptide sequences, predicted MHC binding
115 affinities and gene expression[44] (Fig. 1E; Supplementary Fig. S1C). Loss of MHC class I antigen presentation or
116 responsiveness to IFNγ are established, albeit somewhat rare, mechanisms of ICI resistance[45]. However, each
117 model cell line also maintained the ability to induce MHC-I expression upon IFNγ stimulation (Supplementary
118 Fig. S1D).

119 Notably, when implanted into syngeneic C57BL/6J mice, the tumor models demonstrated contrasting
120 responses to combination ICI treatment of anti-PD-1 and anti-CTLA4, paralleling the observed ICI response rates
121 for human MSI-H cancers[11,15]. The B16F10 melanoma subcutaneous tumors responded to ICIs, where MSI-H
122 tumors were more sensitive to ICIs compared to MSS tumors, although *in vitro* cell doubling times were not
123 different between MSS and MSI-H cells (Fig. 1F and G; Supplementary Fig. S1E and F). The EO771 breast MSS
124 and MSI-H tumors, implanted into the mammary fat pad, also responded to ICIs, with the greatest response seen
125 in MSI-H tumors (Supplementary Fig. S1G-I). However, resistance to ICIs was notable in the MSS or MSI-H

126 LLC tumors in either the subcutaneous space or the mammary fat pad, sites of implantation that result in similar
127 tumor immune composition (Fig. 1H and I; Supplementary Fig. S1J-N).

128 To investigate mechanisms responsible for the divergent ICI responses in these models, we used mass
129 cytometry by time-of-flight (CyTOF), analyzing the immune infiltrate from tumor samples on day 13 post-
130 implantation, where tumor sizes are similar across the models. Identification of major immune cell types in the
131 TME revealed that ICI treatment induced T cell infiltration in both B16F10 and LLC MSI-H tumors (Fig. 1J and
132 K, Supplementary Fig. S2), suggesting that the ICI resistance in the LLC MSI-H model is unlikely to be
133 attributable solely to insufficient numbers of TILs. ICI resistance in T cell-infiltrated tumors was not exclusive to
134 the MSI-H context or the C57BL/6J genotype. EMT6 breast tumors in the mammary fat pad of BALB/cJ mice
135 were also resistant to combination ICIs, despite increased CD8 T cell infiltration following treatment
136 (Supplementary Fig. S3A-C).

137

138 <u>ICI-Resistant Tumors Acquire Unfavorable T cell Activation States After Treatment</u>

139 To define phenotypic differences in TILs in ICI-responsive vs. resistant tumors, we further analyzed
140 antigen-experienced CD44+ CD8 and conventional CD4 T cells (CD4 Tconv) by Uniform Manifold
141 Approximation and Projection (UMAP)[46], and by differential abundance (DA) analysis[47]. This approach enabled
142 identification of cell subsets enriched in each condition and definition of their differentiation and activation states.
143 We focused our analysis to understand the differences between the ICI-treated B16F10 MSI-H and LLC MSI-H
144 tumors. Analysis of day 13 tumor-infiltrating CD8 T cells showed differentially-abundant (DA) cells for each
145 condition (Fig. 2A and B) with distinct marker expression (Fig. 2C). To further quantify the phenotypic
146 differences, DA cells were subsequently grouped by unsupervised clustering. Clusters 4, 5 and 6, which were
147 enriched in B16F10 MSI-H tumors, were notably higher in expression of markers characteristic of activated
148 effector T cells, including Ki67, granzyme B (GrB), CD39, CD38, and PD1. In contrast, cluster 2, which was
149 enriched in LLC tumors, expressed comparatively lower expression of these markers (Fig. 2D and E). LLC tumors
150 were also enriched in cluster 3 cells, which expressed TCF1 but were PD1-, resembling memory precursor-like
151 CD8 T cells that have been shown to demonstrate more polyfunctionality, including TNFα production[48].

152 Quantification of cells with high expression of Ki67, GrB, CD39, CD38, and PD1 by manual gating confirmed
153 the relative paucity of this CD8 T cell subset in LLC MSI-H tumors (Fig. 2F).

154 Analysis of CD44+ CD4 Tconv cells similarly showed DA cells largely separated in UMAP space and
155 protein expression (Fig. 2G-I). Clustering of DA cells revealed clusters 3 and 4, which were enriched in B16F10
156 MSI-H tumors, characterized by high expression of Ki67, PD1, CD39, and CD38 (Fig. 2J and K). Similar to the
157 CD8 T cell subsets, cluster 2 cells enriched in LLC MSI-H tumors were TCF1+ and PD1-. Manual gating of the
158 cell subset corresponding to CD4 clusters 3 and 4 in individual mice confirmed relative depletion in LLC MSI-H
159 tumors (Fig. 2L). We also performed the same analysis including T cells from the ICI-responsive EO771 MSI-H
160 and ICI-resistant EMT6 models in the ICI-treated setting. The EO771 MSI-H tumors, in comparison to the
161 resistant LLC MSI-H or EMT6 tumors, also showed an enrichment in CD8 T cells highly expressing Ki67, GrB,
162 CD39, CD38, and PD1 and CD4 Tconv cells highly expressing Ki67, CD39, CD38, and PD1, similar to the
163 subsets enriched in B16F10 MSI-H tumors, when compared to EMT6 (Supplementary Fig. S4). In sum, these
164 data show that, despite increased T cell infiltration, T cells in the ICI-resistant tumors fail to acquire the activation
165 state and effector marker phenotypes observed in T cells in the ICI-responsive models[44].

166

167 <u>IL-1 and TNFα Synergistically Drive Neutrophil Inflammation via IL1R1-Expressing Tumor Cells</u>

168 Next, we focused on determining cell types and pathways responsible for the divergent T cell states in
169 each model. In both LLC MSS and MSI-H tumors, treatment with ICIs led to higher neutrophil infiltration
170 compared to IgG-treated controls, or B16F10 MSI-H tumors with or without treatment (Fig. 3A). Compared to
171 mice with B16F10 MSI-H tumors, those with LLC MSI-H tumors treated with or without ICIs exhibited
172 significantly more positive or negative pairwise frequency correlations between neutrophil cell subsets and other
173 immune cell subsets across tumor, blood, tumor-draining lymph node and spleen (Fig. 3B), suggesting system-
174 wide coordination we previously described for the LLC model[49]. Sorted neutrophils from ICI-treated LLC MSI-
175 H tumors suppressed OT-I T cell proliferation *in vitro* (Fig. 3C), consistent with the function of
176 polymorphonuclear myeloid-derived suppressor cells (PMN-MDSCs) that are extensively described in the
177 context of cancer[50]. We subsequently examined the cytokine milieu of the TME to understand factors that can

178 drive these changes in the LLC MSI-H tumor-bearing mice. Principal component analysis of cytokines in tumor
179 lysates revealed that ICI treatment resulted in increased levels of cytokines regulated by the NF-κB pathway,
180 including TNFα, IL-1β, G-CSF, and CXCL1 (Fig. 3D, Supplementary Table S3). Indeed, further quantification
181 in tumor lysates confirmed that ICI treatment results in increased amounts of the neutrophil growth factor G-CSF,
182 and neutrophil chemoattractants CXCL1 (Fig. 3E), and CXCL2 (Supplementary Fig. S5A). Quantitative PCR of
183 *Csf3* (coding for G-CSF) and *Cxcl1* transcripts from sorted cells from the TME showed that tumor cells increased
184 expression of both transcripts upon ICI treatment (Fig. 3F; Supplementary Fig. S5B and C, and Supplementary
185 Fig. S12A). These data are consistent with our own prior data and the literature reporting production of G-CSF
186 and CXCL1 from mouse and human tumors[49,51–54] and suggest that ICI treatment further upregulates this existing
187 circuit. Of note, fibroblasts in tumor were also capable of inducing G-CSF transcription following ICIs (Fig. 3F),
188 although in the LLC TME, tumor cells outnumber fibroblasts by 10:1 (Supplementary Fig. S5D).

189 We previously reported that G-CSF production by LLC tumor cells is dependent on signaling through the
190 IL-1 Receptor 1 (IL1R1)[49]. IL-1α and IL-1β, both of which can signal through IL1R1, are known to synergize
191 with TNFα through the canonical NF-κB pathway to upregulate G-CSF, CXCL1 and CXCL2 production, possibly
192 via IL-1-induced increase in TNF receptors[55,56]. In the TME of LLC tumors, we detected both IL-1α and IL-1β,
193 where the former is present in larger quantities while the latter is induced upon ICIs (Supplementary Fig. S5E, F).
194 The transcript for each cytokine increased with ICIs from a mix of tumor and immune cell types (Supplementary
195 Fig. S5G, H). We then confirmed that LLC MSI-H cells and EMT6 cells increase G-CSF and CXCL1 production
196 after stimulation by TNFα and IL-1α *in vitro,* in comparison to minimal responses in B16F10 and EO771 MSI-
197 H tumor cells (Fig. 3G, Supplementary Fig. S6A-D). G-CSF and CXCL1 induction by TNFα plus IL-1α or IL-
198 1β were synergistic, with greater than additive responses seen with the combination (Fig. 3G, Supplementary
199 Figs. S6A-G). Interestingly, maximal synergism for G-CSF production could be achieved with very low levels of
200 IL-1β (1ng/mL), whereas increasing amounts TNFα potentiated the synergy (Supplementary Fig. S6E-H).
201 Turning our attention to the downstream NF-κB pathway, LLC MSI-H cells degraded IκB more significantly
202 compared to B16F10 MSI-H cells, consistent with greater NF-κB pathway activation in the LLC model (Fig. 3H,

203 Supplementary Fig. S6I). Furthermore, the addition of NF-κB inhibitor QNZ suppressed G-CSF and CXCL1
204 expression from LLC tumor cells (Fig. 3I).

205 To understand why LLC and EMT6 cells were more sensitive to stimulation by IL-1 and TNFα, we
206 examined the protein expression of IL1R1 and TNFR1 by flow cytometry. This revealed that LLC MSI-H and
207 EMT6 cells have a high expression of IL1R1 in contrast to minimal expression in B16F10 MSI-H and EO771
208 MSI-H cells, while all cell lines expressed TNFR1 when compared to fluorescence-minus-one controls (Fig. 3J
209 and K; Supplementary Fig. S7A-E). There was no difference in IL1R1 expression between LLC MSS vs. MSI-H
210 cells (Supplementary Fig. S7F). We further investigated IL-1 and TNF pathway gene expression from bulk RNA
211 sequencing data from LLC and B16F10 lines. For IL-1 pathway genes, we found that *Il1r1* was the most
212 differentially regulated gene between the two models, with minimal expression of *Il1r2* and similar expression of
213 *Il1rap* (Supplementary Fig. S7G). When comparing TNF pathway genes, we confirmed similar high expression
214 of *Tnfrsf1a,* coding for TNFR1 (Supplementary Fig. S7H). *Tnfrsf1b* (coding for TNFR2), which can contribute
215 to CXCL1 inflammation[57], was expressed at an overall low level in each model but was slightly increased in LLC
216 cells (Supplementary Fig. S7H). In sum, these data implicate an inflammatory immunosuppressive circuit
217 supporting ICI resistance in tumor types responsive to IL-1 and TNFα stimulation, notable for their expression
218 of IL1R1.

219

220 <u>IL1R1 Perturbation Limits Immunosuppressive Inflammation and Restores Favorable T Cell States to Sensitize</u>
221 <u>Resistant Tumors to ICIs</u>

222 We next evaluated the effect of perturbing this inflammatory axis *in vivo*. Blockade of IL-1 signaling with
223 IL1R1-neutralizing antibody reduced G-CSF and CXCL1 in LLC MSI-H tumors (Supplementary Fig. S8A),
224 decreased neutrophil recruitment to the tumor (Supplementary Fig. S8B), and sensitized LLC MSI-H tumors to
225 treatment with ICIs (Fig. 4A and B; Supplementary Fig. S8C). Importantly, tumor-specific deletion of IL1R1 via
226 CRISPR also sensitized LLC MSI-H tumors to ICIs, implicating tumor-intrinsic IL1R1 signaling during ICI
227 resistance (Fig. 4C and D; Supplementary Fig. S8D). We additionally tested the effect of antagonizing G-CSF,

228 downstream of IL1R1 signaling, via tumor implantation in G-CSF receptor-null mice or injection of G-CSF
229 neutralizing antibody. This showed that loss of host G-CSF receptor signaling depletes neutrophils from tumors
230 and improves tumor control with ICIs, while delivery of G-CSF neutralizing antibody also increases tumor control
231 with ICIs (Supplementary Fig. S8E-J).

232 Next, we performed CyTOF analyses of antigen experienced CD44+ CD8 and CD4 Tconv cells to
233 determine changes in T cell states upon IL1R1 blockade for LLC MSI-H tumors treated with ICIs. DA analysis
234 identified a group of cells enriched in the IL1R1 blockade condition that occupied UMAP space with higher
235 expression of effector T cell molecules such as GrB and CD39, akin to CD8 T cells more frequently found in
236 B16F10 tumors from the previous analysis (Fig. 4E-G; Fig. 2E). Clustering of DA cells highlighted this phenotype,
237 identifying cluster 1, which demonstrated high median expression of Ki67, GrB, CD39, and CD38 (Fig. 4H and
238 I). Quantification by manual gating on individual mice confirmed an increase in this cell subset in the IL1R1
239 blockade group (Fig. 4J). Similarly, we analyzed CD44+ CD4 Tconv cell phenotypes, identifying DA cells in the
240 IL1R1 blockade group that expressed higher levels of effector molecules (Fig. 4K-M). Clustering the DA cells
241 revealed clusters 1 and 2 which were enriched in the IL1R1 blockade group and demonstrating high median
242 expression of Ki67, CD39, CD38, PD1, and GrB (Fig. 4N and O). Manual gating of this cell subset in individual
243 mice confirmed relative enrichment with IL1R1 blockade (Fig. 4P). On the other hand, with IL1R1 blockade we
244 found relative reductions in TCF1+ PD1- CD8 cluster 5 and CD4 cluster 4 T cells, which we previously identified
245 as an enriched subset in LLC MSI-H tumors in comparison to B16F10 MSI-H tumors (Fig. 2E and K). Lastly,
246 we evaluated whether IL1R1 blockade impacts other cell types within the TME in this model, such as tumor-
247 associated macrophages or endothelial cells that can express IL1R1[58,59]. In the LLC MSI-H tumors treated with
248 ICIs, we did not observe significant changes in cell frequencies of CD11b+ F4/80+ tumor-associated macrophages
249 or CD31+ endothelial cells, nor significant changes in the expression of macrophage markers including PD-L1,
250 CD206, CD38, CD39, iNOS, and MHCII (Supplementary Fig. S8K-M). These data collectively show that
251 perturbation of the inflammatory circuit via IL1R1 inhibition sensitizes resistant tumors to ICIs and results in a
252 shift of CD8 and CD4 T cells to cytotoxic effector-like states.

253

254 T Cells Drive the Inflammatory ICI Resistance Circuit via TNFα

255 Because this inflammatory circuit was intensified by ICIs in LLC MSI-H tumors in association with T
256 cell infiltration, and activated T cells are well-known to produce TNFα[60], we hypothesized that T cells may
257 paradoxically exacerbate the inflammatory resistance program when infiltrating into a TME with an active NF-
258 κB inflammatory circuit. Depleting T cells in LLC MSI-H tumors using an anti-Thy1 antibody significantly
259 decreased G-CSF and CXCL1 protein levels as well as neutrophil infiltration in the TME (Fig. 5A-C). Although
260 Thy1 can be expressed in fibroblasts, they were not significantly depleted in LLC MSI-H tumors upon anti-Thy1
261 treatment (Supplementary Fig. S9A). Additionally, using anti-CD4 plus anti-CD8 antibodies for T cell depletion
262 phenocopied aThy1 treatment to reduce G-CSF, CXCL1 and neutrophils, requiring elimination of both T cell
263 types (Supplementary Fig. S9B and C). CD4 and CD8 depletion in the EMT6 model also reduced tumor-
264 infiltrating neutrophils (Supplementary Fig. S9D). These results support a role for T cells in driving the
265 inflammatory ICI resistance circuit.

266 We next sought to directly test the interaction between T cells and tumor cells, hypothesizing that T cell-
267 derived TNFα can stimulate tumor cells to produce inflammatory cytokines that support neutrophils. Co-culturing
268 CD3/CD28-stimulated CD8 T cells sorted from LLC MSI-H tumors together with LLC MSI-H tumor cells
269 increased G-CSF production as quantified in the supernatant by more than five-fold, indicating that CD8 T cells
270 are sufficient to drive this circuit (Fig. 5D and E; Supplementary Fig. S12B). Importantly, the increase in G-CSF
271 was largely dependent on TNFα, as the addition of a neutralizing antibody to TNFα resulted in a significant
272 reduction of G-CSF (Fig. 5E). Neutralization of other potential T cell factors, such as FasL or GM-CSF, did not
273 result in reduction of G-CSF (Supplementary Fig. S9E). *In vivo*, treatment with ICIs specifically increased TNFα-
274 expressing CD4 and CD8 T cells in LLC MSI-H tumors compared to the spleen (Fig. 5F). This was also
275 accompanied by ICI-induced increases in TNFα+ tumor-infiltrating neutrophils, a cell type well-known to express
276 TNFα[61] (Supplementary Fig. S9F). CD4 and CD8 depletion decreased TNFα+ neutrophils in the TME
277 (Supplementary Fig. S9G), demonstrating dependence on T cell activity. Further characterization of TNFα+ CD8
278 T cells revealed that these cells are less likely to express Ki67 or GrB in comparison to TNFα- cells (Fig. 5G and

279 H), segregating these key effector functions into different T cell subsets. Analysis of TNFα+ CD4 T cells also
280 showed lower expression of Ki67, though these cells demonstrated higher expression of CD39 (Supplementary
281 Fig. S9H).

282 To test the functional contribution of TNFα to the inflammatory ICI resistance circuit, we implanted LLC
283 MSI-H tumors in *Tnf* knockout mice lacking host-derived TNFα, which sensitized the tumors to ICI treatment
284 accompanied by a decrease in neutrophils (Fig. 5I and J; Supplementary Fig. S9I and J). Furthermore, we
285 generated T cell-specific *Tnf* knockout mice as previously described, using *Cd4*-cre to delete the *Tnf(fl/fl)* allele[61]
286 (Supplementary Fig. S9K-M). Importantly, tumor growth was also restricted following ICIs in mice specifically
287 lacking T cell-derived TNFα (Fig. 5K and L; Supplementary Fig. S9N). We further evaluated the impact of IL1R1
288 blockade in the setting of T cell TNFα loss, hypothesizing that, given the synergy between IL-1 and TNFα, we
289 would not observe an additive benefit with the combined perturbations. Indeed, tumor control with ICIs with the
290 combination of IL1R1 blockade and T cell TNFα knockout was not significantly different from the benefit with
291 single perturbation alone (Supplementary Fig. S9O-Q). Collectively, these data support a novel mechanism
292 whereby ICI-induced infiltration of T cells producing TNFα exacerbates NF-κB-driven transcription of G-CSF
293 and CXCL1 in tumor cells to create a paradoxical circuit of immunosuppression.

294

295 <u>T cell, Tumor, and Neutrophil Inflammation Circuit Is Active in Human Cancer and Is Associated with Poor</u>
296 <u>Clinical Outcome</u>

297 We next interrogated our model of T cell-exacerbated tumor inflammation in human cancer. First, we
298 tested whether G-CSF and CXCL1 production can be elicited from human cancer cells. We incubated breast
299 cancer organoids derived from two different resected primary tumors (TORG40, isolated from triple-negative
300 inflammatory breast cancer, and TORG139, isolated from triple-negative breast cancer) with IL-1α and TNFα.
301 The TORG40 organoids demonstrated significant induction of G-CSF and CXCL1 secretion in the supernatant,
302 while the TORG139 organoids did not produce G-CSF and had a diminished induction of CXCL1 in comparison
303 (Fig. 6A and B). RT-qPCR showed that TORG40 organoids also had a higher induction of *CXCL8* transcripts

304 compared to TORG139 (Supplementary Fig. S10A). Based on our mouse data, we hypothesized that TORG40
305 cells expresses *IL1R1* more highly compared to TORG139 cells. Indeed, TORG40 cells had higher *IL1R1* but
306 similar *TNFR1* expression compared to TORG139 cells (Fig. 6C; Supplementary Fig. S10B). These data further
307 support our findings in mouse tumor cells that IL1R1 expression distinguishes tumors sensitive to IL-1 and TNFα
308 stimulation.

309 To understand the relationship between T cells and tumor cells in more detail in the context of ICI
310 treatment, we analyzed a publicly available single-cell RNA sequencing dataset of tumor samples from non-
311 metastatic breast cancer patients before and after a single dose of pembrolizumab[62] (Fig. 6D). A total of 7 clusters
312 were identified across all CD8 T cells (Fig. 6E; Supplementary Fig. S10C). Notably, we observed a separation of
313 CD8 T cells expressing *TNF* from those expressing GrB (*GZMB),* or Ki67, which was expressed by cells in the
314 Activated/proliferating cluster (Fig. 6F; Supplementary Fig. S10C), paralleling the results from our mouse models
315 (Fig. 5G and H). Comparison of differentially expressed genes in the two *TNF*-expressing clusters –
316 *TNF*+*GZMK*+ and *TNF*+ *IFNG*+ exhausted – to the *GZMB*+ exhausted cluster revealed higher expression of
317 markers suggestive of activation (*CD69*[63]*, FOS*[64]*, DUSP1*[65]*,* and *CCL4*[66]*;* Supplementary Fig. S10D and E).
318 Importantly, we found that the *TNF*+ *GZMK*+ cluster and *TNF*+ *IFNG*+ exhausted cluster significantly increased
319 in patients following pembrolizumab treatment, whereas the *GZMB*+ Exhausted cluster was not significantly
320 changed (Fig. 6G-I, Supplementary Fig. S10F). The increases in the *TNF*-expressing clusters were positively
321 correlated with each other (Supplementary Fig. S10G). We additionally examined *TNF* expression from CD4 T
322 cells and myeloid cells in this dataset. For CD4 T cells, a variety of subsets expressed *TNF,* ranging from Th0,
323 Th1, and Th17 cells (Supplementary Fig. S11A-C). Among these, *TNF*+ Th1 subsets increased following ICI
324 treatment, characterized by expression of *ENTPD1* (coding for CD39), which we previously noted to be expressed
325 highly by TNFα+ mouse CD4 T cells (Supplementary Figs. S11D and E, and S9H). For myeloid cells, a portion
326 of C1q+ macrophages expressing *TNF* increased following treatment (Supplementary Fig. S11F-I).

327 Next, we hypothesized that in the setting of an increase in *TNF*-expressing cells with ICIs, *IL1R1*-
328 expressing tumors would preferentially activate tumor-intrinsic NF-κB inflammation. For tumor cells in each

329 patient sample, we determined the level of *IL1R1* expression as well as tumor cell-specific score of NF-κB activity
330 based on an established gene set[67]. Tumor NF-κB scores were higher in the IL1R1-high group of patients
331 following ICIs (Fig. 6J). Furthermore, increases in the CD8 *TNF*+ *GZMK*+ and *TNF*+ *IFNG*+ exhausted cluster
332 frequencies were positively correlated with increases in tumor NF-kB scores in the IL1R1-high group, but not in
333 the IL1R1-low group (Supplementary Fig. S11J). These results demonstrate that ICI treatment can induce an
334 expansion of inflammatory leukocytes characterized by *TNF* expression that are associated with increased tumor-
335 intrinsic NF-κB signaling when the tumor cells express *IL1R1*.

336 Because droplet-based single-cell RNA-sequencing does not efficiently capture neutrophils[68], we sought
337 to test our hypotheses regarding neutrophils using additional human datasets containing neutrophil quantification.
338 Recently, a multicellular and molecular inflammatory hub composed of NF-κB transcription factors,
339 inflammatory tumor cells, lymphocytes, neutrophils, and neutrophil-attracting chemokines has been described in
340 human colorectal cancer (COAD)[69]. We hypothesized that within a TME capable of upregulating such NF-κB-
341 dependent, neutrophil-recruiting inflammation, MSI-H status and the accompanying increased T cell
342 infiltration[70,71] would result in an increase in neutrophils in the TME. Inference of TME immune composition
343 using CIBERTSORTx[72] for analysis of the Cancer Genome Atlas (TCGA) RNA sequencing dataset for COAD
344 patients, grouped by their MSI status, showed an increase in neutrophils in a subset of MSI-H tumors compared
345 to MSS tumors (Supplementary Fig. S11K). We reasoned furthermore that, given the systemic mobilization of
346 neutrophils during ICI resistance in antigen-rich tumors in mice, ICI resistance in patients with MSI-H cancers
347 may be associated with exacerbated systemic neutrophilia after treatment. We identified MSI-H cancers in our
348 institutional clinical next-generation sequencing database and analyzed those who were started on ICI therapy but
349 experienced treatment failure. When compared to a 6-week period prior to initiation of ICIs, the peripheral blood
350 neutrophil to lymphocyte ratio (NLR) was increased after ICI treatment in the period preceding disease
351 progression (Fig. 6K). On the other hand, for patients who did not experience progression, NLR did not change
352 over the same interval of time. NLR has been associated with poor prognosis in various human cancer types,
353 including but not exclusive to MSI-H cancers[73,74].

354 Lastly, we determined the significance of the T cell-tumor-neutrophil inflammatory circuit with regard to
355 clinical outcomes for ICI-treated patients. To this end, we analyzed RNA sequencing data from the atezolizumab
356 arm of the OAK trial (NCT02008227), which was a randomized phase III trial comparing atezolizumab vs.
357 docetaxel in locally advanced or metastatic non-small cell lung cancer patients[75,76]. Following stratification of
358 patients into *CD8A* high vs. low groups, we determined the impact of a custom gene set score "inflam" consisting
359 of genes involved in the ICI resistance circuit we have described, including *IL1R1, TNFRSF1A, IL1A, IL1B, TNF,*
360 *CD69, CSF3, CXCL1, CXCL2, CXCL8, NFKB1, NFKB2.* This analysis demonstrated that only patients in the
361 CD8A high but "inflam" low group had superior overall survival compared to the other groups in aggregate
362 (p=0.00124; HR=1.667 (1.222-2.278)), as well as to each individual group (CD8A high, "inflam" high: p=0.0273,
363 HR=1.517 (1.048-2.196)); CD8A low, "inflam" low: p=0.0113, HR=1.634 (1.117-2.392); and CD8A low,
364 "inflam" low p=0.00089, HR=1.8642 (1.291-2.692)) (Fig.6L). Notably, those patients with CD8A high and
365 "imflam" high tumors, similar to our resistant mouse models, did not experience a survival benefit. Analysis of
366 progression-free survival (PFS) demonstrated similar trends, with patients in the CD8A high but "inflam" low
367 group exhibiting the most favorable outcomes (Supplementary Fig. S11L). These data provide additional evidence
368 in support of the proposed ICI resistance mechanism in tumors with T cell infiltration (Fig. 6M).
369

370 **Discussion**

371 In this study, we define a mechanism by which T cells exacerbate an inflammation circuit involving NF-
372 κB pathway activation in IL1R1+ tumor cells, paradoxically driving an immunosuppressive TME characterized
373 by neutrophil recruitment and resistance to ICI therapy. NF-κB is a signaling pathway activated in many cell
374 types in the TME and is known to both promote and prevent tumor progression depending on context[19]. NF-κB
375 signaling in cancer and myeloid immune cells, however, frequently results in pro-tumor inflammation during
376 tumorigenesis and progression[77,78]. Notably, inhibition of TNFα has recently been shown to improve ICI efficacy
377 in mouse models, in addition to protecting against autoimmune adverse effects[35,36]. However, TNFα can be
378 produced by many cell types[61], and therefore it has remained unclear to what extent T cells contribute to the

379 effects of TNFα inhibition against cancer. Our data show that T cell-derived TNFα can potentiate the production
380 of NF-κB-regulated soluble factors that promote adaptive resistance to therapy in IL1R1-expressing tumors.

381 Prior publications have highlighted the importance of an immunosuppressive axis involving
382 immunosuppressive neutrophils (PMN-MDSCs) that are critically relevant for cancer treatment outcome[50].
383 Notably, the Melero and Datta groups have recently reported IL-1 and TNF can promote CXCL1, CXCL2 and
384 IL-8 (in humans) from tumor cells and fibroblasts, culminating in PMN-MDSC recruitment to the TME[57,79]. Our
385 results build on these recent findings, and we now provide new functional data demonstrating a paradoxical role
386 for T cell-derived TNFα in exacerbating this inflammatory resistance circuit after ICI treatment. In cancer
387 immunity, various T cell subsets have been implicated in tumor development and progression, most notably Tregs,
388 which classically suppress effector T cell responses[80]. Th17 CD4, as well as γδ T cells, can also drive pro-tumor
389 inflammation via IL-17 production[81,82], while CD8 T cells have been previously shown to promote chemical
390 carcinogenesis[83,84]. Interestingly, in the context of autoimmunity and immune-related adverse events, effector
391 memory CD4 T cells have been recently shown to instruct NF-κB inflammation in partnering dendritic cells in a
392 TNFR- and CD40-dependent manner[85,86]. We now show that ICI treatment can result in CD4 and CD8 T cell-
393 exacerbated immunosuppressive inflammation, mediated by T cell-derived TNFα, which synergizes with IL-1
394 present in the tumor microenvironment to limit therapeutic efficacy. This adds nuance to the prevailing view that
395 T cell effector functions are beneficial in the TME and for response to immunotherapy, distinguishing productive
396 from detrimental effector functions that depend on the context of the tumor. Our data importantly demonstrate
397 that tumor cells expressing IL1R1 can best participate in the immunosuppressive circuit due to synergistic
398 activation of NF-κB by IL-1 and TNFα.

399 While we have focused on the role of IL-1 and TNFα in signaling through tumor cells to elicit
400 immunosuppressive neutrophilic inflammation, it is important to note that there may be a number of
401 complementary mechanisms through which these cytokines amplify immune suppression in the TME. IL1R1
402 expression on host cells, including fibroblasts, has been shown to contribute to accumulation and potentiation of
403 MDSC activity[87,88]. In addition, TNFα can act directly on cells in the TME to promote tumor progression,

404 including induction of T cell activation-induced cell death[89,90], tumor cell dedifferentiation[91], and stabilization of
405 immunosuppressive molecules such as PD-L1, CD73, CD39, and TGF-β, which can potentiate CD4 Treg
406 function[33,92]. Our own data specifically provide support for the function of tumor cell-expressed IL1R1 and T
407 cell-derived TNFα toward ICI efficacy, and additional experiments are needed to dissect the contribution and
408 interaction of each of these intersectional mechanisms.

409 While we have leveraged T cell-infiltrated MSI-H tumors for our study, the mechanism presented is not
410 specific to MSI-H tumors. We show the ICI resistance circuit is also active in the EMT6 breast cancer model
411 (which does not exhibit MSI), breast cancer organoids, and in non-MSI breast and lung cancer. Rather than MSI
412 status, the common denominators for engaging the resistance circuit are recruitment of TNF-expressing T cells,
413 presence of IL-1, and expression of IL1R1 on tumor cells, which collectively result in activation of the NF-κB
414 pathway to drive neutrophil recruitment. In patients, our results indicate that neutrophil predominance as
415 quantified by NLR is associated with ICI resistance in MSI-H tumors and that a gene signature of this resistance
416 circuit is correlated with ICI treatment outcome in lung cancer patients, whose tumors rarely display MSI-H
417 status[93]. We hypothesize that the increased antigenic burden in MSI-H tumors can exacerbate T cell-mediated
418 inflammation in tumors responsive to IL-1 and TNFα, although we do not rule out potential contribution from
419 immune-stimulatory effects of genome instability induced by MMRd[94,95].

420 Importantly, our study revises the prevailing paradigm of ICI efficacy and offers a potential explanation
421 for why patients may experience poor responses to ICIs despite predicted or confirmed T cell infiltration, beyond
422 T cell exhaustion. Importantly, while high T cell infiltration or proxy measures for T cell inflammation such as
423 high tumor mutational burden or MMRd/MSI-H status generally correlate with a relative improvement in ICI
424 responses as compared to non-T cell inflamed controls, it is notable that often, the majority of patients in the high
425 T cell inflammation group still do not respond to therapy[11,12,96]. Our findings now refine the current models of
426 ICI response to include the active role that tumor-infiltrating CD4 and CD8 T cells can play in shaping the
427 inflammatory tone of the TME, including unexpectedly exacerbating an immunosuppressive tissue environment.

428 Strategies targeting the IL-1/IL1R1/TNF axis are being tested in clinical trials. Based on the finding that
429 IL-1β inhibition via Canakinumab may have reduced lung cancer incidence and mortality, a series of phase III
430 CANOPY clinical trials were launched and recently reported their results, albeit demonstrating no significant
431 impact on survival outcomes during treatment of non-small cell lung cancer with inhibition of IL-1β alone[97–100].
432 A phase I-II trial is ongoing to test the safety and efficacy of an IL1R1 inhibitor Isuanakinra in combination with
433 ICIs in patients with advanced solid tumors (NCT04121442). The combination of TNF inhibitors Infliximab or
434 Certolizumab with Nivolumab and Ipilimumab was recently tested in the TICIMEL phase Ib trial in patients with
435 advanced or metastatic melanoma, with a good safety profile and promising response rate[101]. Lastly, an inhibitor
436 of CXCR1 and CXCR2, which are receptors for neutrophil chemokines including CXCL1, CXCL2, and CXCL8,
437 is being tested in combination with ICIs in patients with melanoma, non-small cell lung cancer, and colorectal
438 cancer (NCT03161431, NCT05570825, NCT04599140). Our results contribute to the rationale for these ICI
439 combination approaches, and further suggest that a subset of patients who could particularly benefit from ICIs
440 and IL1R1/TNFα blockade may be those with T cell-infiltrated tumors and $IL1R1^{+}$ tumor cells. Lastly, we provide
441 evidence for G-CSF/G-CSFR inhibition as a potential therapeutic strategy in combination with ICIs, an approach
442 that has not yet entered clinical trials.

443 In summary, our data elucidate a mechanism by which T cells can unexpectedly promote ICI resistance
444 in a manner dependent on the tumor context. These results can inform new strategies for therapy selection and
445 immune monitoring as well as therapeutic strategies to convert inflammation-promoting T cell activity into
446 productive anti-tumor immunity.

447

448 **Methods**

449 Cell lines

450 Parental LLC cells (RRID:CVCL_4358) were gifted by Dr. Ross Levine (Memorial Sloan Kettering
451 Cancer Center). B16F10 cells (RRID:CVCL_0159) were gifted by Dr. Jeffrey Bluestone (University of California,
452 San Francisco (UCSF)). EO771 cells (RRID:CVCL_GR23) were gifted from Dr. Robin Anderson (Peter
453 MacCallum Cancer Center). EMT6 cells (RRID:CVCL_1923) were purchased from ATCC. LLC, B16F10, and

454 EO771 parental and derivative cell lines were cultured in DMEM supplemented with 10% fetal calf serum, 10mM
455 HEPES, and 100 U mL^{-1} penicillin and 100 µg mL^{-1} streptomycin. EMT6 cell lines were cultured in Waymouth's
456 MB 752/1 medium with 2mM L-glutamine, 15% fetal calf serum and 100 U mL^{-1} penicillin and 100 µg mL^{-1}
457 streptomycin. For generation of MSH2 and IL1R1 knock out cell lines, a combination of two targeting guide
458 crRNAs (Dharmacon), or scrambled nontargeting control, were mixed with tracrRNA and recombinant Cas9
459 protein (QB3 Macrolab, UC Berkeley) at 1:1:2:2 molar ratio and incubated at 37°C to form the ribonucleoprotein
460 complex. This was then mixed with 1ul of 100uM single-stranded oligodeoxynucleotides (ssODN) enhancer, and
461 3 x 10^5 trypsinized cells in electroporation buffer and electroporated using the Lonza 4D 96-well electroporation
462 system. Nucleic acid sequences, electroporation buffer type and electroporation code are found in Supplementary
463 Table 1. After a 15 minute recovery in a 37°C CO2 incubator, cells were expanded in culture at subculture ratios
464 of 1:10-1:15 every 48 hours. MSI-H cell lines used have undergone 60 passages in total. All cell lines underwent
465 mycoplasma testing with negative results as of November 1, 2023. Cells were used for experiments within 2-3
466 passages of thaw.

467 Following the initial experiments included in this manuscript, cell line verification testing was performed
468 via short tandem repeat (STR) analysis on the syngeneic mouse tumor cell lines used. All cell lines were
469 successfully matched, but it revealed that a cell line we had previously attributed to be the AT3 breast cancer cell
470 line (RRID:CVCL_VR89) was in fact the LLC cell line (RRID: CVCL_4358), along with its MSS and MSI-H
471 derivative lines[49]. To further ensure that the cell line was correctly identified as LLC, we performed a PCR assay
472 for PyMT transgene detection, which should be present in the AT3 line because it was derived from an MMTV-
473 PyMT mouse[102]. We confirmed this to be true in an independently purchased reference AT3 cell line, now
474 available from Millipore, but not in our LLC cell lines (Supplementary Figs. S2, and S13). Furthermore, we used
475 exome sequencing data from our cell line to verify the presence the of two point mutations reported in the literature
476 to be found in the LLC line[103,104] (Supplementary Table S4).

477

478 <u>Animals and *in vivo* treatments</u>

479 All mice were housed in an American Association for the Accreditation of Laboratory Animal Care-
480 accredited animal facility and maintained in specific pathogen-free conditions. Animal experiments were
481 approved by and conducted in accordance with Institutional Animal Care & Use Program protocol AN184195.
482 Female C57BL/6J (RRID:IMSR_JAX:000664) and BALB/cJ (RRID:IMSR_JAX:000651) mice between 8 and
483 12 weeks old were purchased from the Jackson Laboratory. B16F10 (1 x 10^5 cells per 100 µL), LLC (5 x 10^5 cells
484 per 100 µL), EO771 (8 x 10^6 cells per 100 µL), and EMT6 (5 x 10^5 cells per 100 µL) cells in serum-free DMEM
485 were transplanted into the right subcutaneous flank for B16F10 melanoma, the left 4th mammary fat pad for
486 EO771 and EMT6, and either the flank or the mammary fat pad for LLC. Unless indicated as in Figure 1 and
487 Supplementary Fig. S1 for subcutaneous implantation, LLC cells were implanted into the mammary fat pad for
488 all experiments. Different cell numbers for inoculation were chosen for each model to address disparities in *in*
489 *vivo* tumor growth rates. TCR transgenic OT-I CD45.1 mice (RRID:IMSR_JAX:003831) were bred at our facility.
490 Female B6.129S-*Tnf*^{tm1Gkl}/J mice (RRID:IMSR_JAX:005540, *Tnf-/-* in manuscript), and B6.129X1(Cg)-
491 *Csf3r*^{tm1Link}/J mice (RRID:IMSR_JAX:017838, *Csf3r-/-* in manuscript) between 7-8 weeks of age were purchased
492 from the Jackson Laboratory. For T cell-specific *Tnf* knockout mice, *Tnf(fl/fl)* mice[61] crossed to the Ai14 Cre
493 reporter (RRID:IMSR_JAX:007914) were obtained (gift from Dr. Ophir Klein); these mice were crossed to *Cd4-*
494 cre mice (RRID:IMSR_JAX:022071) to obtain T cell-specific *Tnf* knockout mice. Control *Cd4-cre(WT)* mice
495 included mice with *Tnf(fl/fl)* or *Tnf(fl/+)* genotypes. All mice were heterozygotes or homozygotes for the Ai14
496 Cre reporter allele. Animals were housed under standard specific pathogen-free conditions with typical light/dark
497 cycles and standard chow.

498 For all anti-PD-1 and anti-CTLA4 antibody treatments, 250 µg of anti-PD-1 clone RMP1-14 (Bio X Cell,
499 RRID:AB_10949053) and 200 µg of anti-CTLA4 clone 9H10 (Bio X Cell, RRID: AB_10950184) in 100 µL PBS
500 were injected intraperitoneally at days 3, 6, 9 and 12 post tumor injection. For IL1R1 inhibition, 200 µg of
501 antibody clone JAMA-147 (Bio X Cell, RRID: AB_2661843) was injected intraperitoneally every 3 days starting
502 at day 3 post tumor injection. For Thy1 depletion, 200 µg of antibody clone M5/49.4.1 (Bio X Cell, RRID:
503 AB_1107681) was injected intraperitoneally at days -2, 0, 7 and 14 relative to tumor injection. For anti-CD4
504 (RRID: AB_1107636) and anti-CD8 (RRID: AB_1125541) antibody treatments, 400 µg of each antibody was

505 injected intraperitoneally on days -1, 3, 7, 10, 13, and 16 post tumor injection. Where indicated by "IgG", isotype-
506 matched control IgG antibodies were used at the same concentrations as experimental antibodies (RRID:
507 AB_1107769, AB_1107782). For G-CSF neutralization, 10 ug of antibody (R&D Systems MAB414, RRID:
508 RRID:AB_2085954) was injected intraperitoneally starting at day 5 post tumor implantation.
509
510 MSI PCR quantification
511 Microsatellite instability in the mouse cell lines was quantified using a panel detecting four microsatellite
512 markers[43]. Genomic DNA from cell pellet was isolated using the GeneJET Genomic DNA Purification Kit
513 (Thermo Fisher Scientific, K0722) according to manufacturer protocol. 20 ng of genomic DNA was used as input
514 for a PCR reaction using Platinum Taq (Thermo Fisher Scientific, 10-966-018) with 2mM MgCl2, 0.2 μM each
515 primer (Supplementary Table 2), and 200 μM dNTP. The cycling profile included: 1 cycle at 94 °C for 4 minutes,
516 94 °C for 30 seconds, 56 °C for 45 seconds and 72 °C for 30 seconds for a total of 35 cycles, and a final extension
517 at 72 °C for 6 minutes. Samples were submitted for fragment analysis by Genewiz, and analyzed using
518 PeakScanner 2 (Thermo Fisher Scientific).
519
520 Next generation sequencing and neoantigen priority score analysis
521 Whole exome and bulk RNA sequencing were performed with flash frozen cell pellet submitted to
522 MedGenome (Foster City, CA). For whole exome sequencing, the library was prepared using the Agilent
523 SureSelectXT Mouse All Exon Kit, and sequenced on NovaSeq 6000 with paired-end 100 read length. Data was
524 processed using Fastq preprocessing using FastQC v0.11.8 and adapter trimming with fastq-mcf v1.05. 99.66%
525 of the total reads aligned to the reference genome. 87.77% of the aligned reads passed the alignment filter
526 (mapping quality ≥ 29 and insert size between 100-1000). Reads after duplicate removal, indel realignment and
527 recalibration featured more than 98.49% coverage and 86.67-114.47X average depth. Somatic variant calling was
528 performed using Strelka[105] (v2.9.10). Default settings were used for variant calling. For realignment and base-
529 recalibration, dbsnp150 variants were used. The identified somatic variants were further filtered and only passed
530 and on-target variants were considered for downstream analysis. Default parameters provided by Strelka were

531 used to filter passed somatic variants. The on-target variants were filtered based on the coordinates of the target
532 regions provided by the vendor. RNA sequencing was performed using two biological replicates per cell line
533 using Illumina TruSeq Stranded Total RNA library preparation, and sequenced using NovaSeq with target of 50
534 million total reads per sample. 86.18-91.46% of total reads for each sample had Quality scores of > 30. Kallisto[106]
535 (v0.46.1) was used to quantify abundances of the transcripts in transcripts per million (TPM) with the strand
536 specific read processing argument '--rf-stranded'.

537 For neoantigen priority score analysis, the MuPeXI pipeline was used as described[44]. The somatic allele
538 frequency estimate was extracted from the strelka vcf records following the Strelka user guide and added to the
539 vcf files. The vcf files with allele frequency, the mean expression output files from Kallisto and the GRCm38
540 references were given as input to the MuPeXI pipeline (v1.2.0) with the species option set to mouse and the HLA
541 alleles set to 'H-2-Kb,H-2-Db'.

542

543 Mass cytometry antibodies

544 All mass cytometry antibodies and staining concentrations are listed in Supplementary Table S5. Primary
545 conjugates of mass cytometry antibodies were prepared using the Maxpar antibody conjugation kit (MCP9 for
546 Cadmium or X8 for non-Cadmium metals; Fluidigm) according to the manufacturer's recommended protocol.
547 After labeling, antibodies were diluted in HRP-Protector Peroxidase Stabilizer (Candor) for Cadmium conjugated
548 antibodies, and Candor PBS Antibody Stabilizer supplemented with 0.02% sodium azide for non-Cadmium
549 conjugated antibodies. Antibodies were stored at 4°C long term. Each antibody clone and lot were titrated to
550 optimal staining concentrations using primary mouse samples.

551

552 Cell preparation

553 Tissue preparations from tumor, tumor-draining lymph node, spleen and lymph node were performed
554 simultaneously. After euthanasia by CO2 inhalation, peripheral blood was collected via cardiac puncture and
555 transferred into heparin-coated vacuum tubes. Blood was diluted into ACK lysis buffer, incubated for 3 minutes
556 on ice then quenched with 10 mL PBS with 5 mM ethylenediaminetetraacetic acid (EDTA) and 0.5% bovine

557 serum albumin (BSA) (PBS/EDTA/BSA). Spleens and tumor-draining inguinal lymph nodes were homogenized
558 with a syringe pusher over 70 µm filter with PBS/EDTA. Tumors were finely minced and digested in RPMI-1640
559 with 4 mg ml^{-1} collagenase IV (Worthington) and 0.1 mg ml^{-1} DNaseI (Sigma) in a scintillation vial with a micro
560 stir bar for 30 minutes at 37 °C. After digestion, cells were filtered twice over 70 µm filters with PBS/EDTA. All
561 tissue samples were centrifuged at 500 *g* for 5 minutes at 4°C, resuspended in PBS/EDTA, and mixed 1:1 with
562 PBS/EDTA containing 100 mM cisplatin (Enzo Life Sciences) for 60 seconds before quenching 1:1 with
563 PBS/EDTA/BSA. Cells were centrifuged again, resuspended in PBS/EDTA/BSA at a density between 1 x 10^6
564 and 1 x 10^7 cells per mL, fixed for 10 minutes at room temperature using 1.6% formaldehyde (final), washed
565 twice with PBS/EDTA/BSA and frozen in 100ul buffer at -80°C. All samples were processed on ice with buffers
566 at 4 °C.
567
568 Mass cytometry
569 2 x 10^6 cells from tumor and 1 x 10^6 cells from other organs from each animal were barcoded with distinct
570 combinations of stable Pd isotopes in 0.02% saponin in PBS as previously described[107]. Cells were washed twice
571 with cell-staining media (PBS with 0.5% BSA and 0.02% NaN_3) and combined into a single 15 mL conical tube.
572 For staining, cells were resuspended in cell-staining media, blocked with FcX (Biolegend, RRID: RRID:AB
573 1574975) for 5 minutes at room temperature, then incubated for 30 minutes at room temperature on a shaker, with
574 surface marker antibody cocktail (Supplementary Table S5) in 1 mL total volume for tumor, and 500 µL volume
575 for other organs. Cells were washed in cell-staining media then permeabilized with methanol for 10 minutes at
576 4 °C, then washed again in cell-staining media. Cells were then incubated with the intracellular antibody cocktail
577 in the same volume as surface markers for 30 minutes at room temperature on a shaker. Cells were washed in
578 cell-staining media then incubated with 1 mL PBS containing 1:5000 Iridium intercalator (Fluidigm) and 4% final
579 formaldehyde. Cells were maintained in this final buffer for 2 days prior to sample acquisition on a CyTOF 2
580 mass cytometer (Fluidigm) using Maxpar Cell Acquisition Solution. 1-5 x 10^5 cells were acquired per each sample.
581 Data normalization was performed using EQ Four Element Calibration Beads (Fluidigm) included during sample

582 acquisition, using Normalizer v0.3 (Nolan lab). Debarcoding was performed using Single Cell Debarcoder v0.2
583 (Nolan lab).
584
585 Mass cytometry data analysis
586 Immune cell subsets were manually gated using the strategy shown in Supplementary Fig. S2. Input cells
587 for DAseq were exported from manually gated cells, with the same number of cells imported per sample. UMAP
588 dimensionality reduction[46] using the package "uwot" (v.0.1.16) was performed using all available protein markers
589 except Ki-67. Differential abundance analysis (DA analysis) was performed using the package "DAseq" (v.1.0.0)
590 using the top 10 principal components determined from the asinh expression for each marker for each cell. Top
591 DA cells were determined by thresholding cells with positive or negative DA measures beyond the extent of
592 random distribution.
593 For pairwise correlation analysis involving neutrophil clusters, clusters were first identified using UMAP
594 and Phenograph[108] using cells from each organ, with manual annotation of clusters representing neutrophils. Cells
595 from LLC MSI-H or B16F10 MSI-H tumor bearing animals were used for further analysis. For each sample, the
596 cluster frequencies were calculated (percent of total singlets for tumor, and percent of live CD45+ cells for other
597 organs). Spearman pairwise correlation was performed as previously described[49], and filtered for correlations
598 involving neutrophils with $r > 0.7$ or < -0.7.
599 For most analyses, batch correction was not applied as aliquots of the same antibody cocktail was used to
600 acquire the entire dataset for analysis. Data in Supplementary Fig. S4 required comparison across experiments
601 acquired separately with antibody cocktails generated at different times. For this analysis, batch correction was
602 applied using the package CyCombine (v. 0.2.16) using an anchor sample common across the two CyTOF runs.
603 For quantification of immune subsets, cells were quantified as a percentage of total singlets, including live
604 and dead cells, and CD45+ and CD45- cells, to reflect the density of that cell type among cells comprising the
605 harvested organ.
606
607 Cytokine quantification

608 For quantification of cytokines from tumor, minced tumor was lysed using RIPA buffer containing
609 protease inhibitor (Cell Biolabs) on ice for 10 minutes, followed by centrifugation at 14,000 rpm for 10 minutes
610 at 4 °C. Supernatant containing cell lysate was collected and normalized to the same A595 using the Bio-Rad
611 Protein Assay. Samples were frozen and stored at -80 °C until quantification. For quantification of cytokines from
612 plasma, freshly isolated peripheral blood was centrifuged for 10 minutes at 4 °C at 1000 *g*. 100 μL of supernatant
613 plasma was mixed 1:1 with 100 μL of PBS/EDTA, and frozen until quantification. For multiplex cytokine
614 quantification, lysates or plasma were submitted for mouse discovery assays available through Eve Technologies
615 (Calgary, AB). For G-CSF and CXCL1 ELISA, tumor lysates were analyzed using the mouse G-CSF ELISA Kit
616 (Abcam ab197743) and CXCL1 ELISA Kit (Abcam ab216951) per manufacturer protocol. Principal component
617 analysis was performed using cytokine concentrations as input. Values were log adjusted then analyzed using the
618 function PCA from the R package FactoMineR[109] (v2.4). Synergy analyses were performed using SynergyFinder
619 Plus web interface (synergyfinder.org[110]), following normalization of G-CSF concentrations with 100%
620 representing the maximum value for each cell line.
621
622 Flow cytometry and cell sorting
623 All flow cytometry antibodies and concentrations used for analysis is found in Supplementary Table S6.
624 Tissue samples were initially processed as for CyTOF, and cells were stained for viability with Zombie-NIR stain
625 (Biolegend). Cell surface staining was performed in cell-staining media (PBS with 0.5% BSA and 0.02% NaN_3)
626 for 20 minutes at room temperature. For intracellular staining, cells were permeabilized and fixed using
627 eBioscience Foxp3/Transcription Factor Staining Buffer Set prior to staining in 1X permeabilization buffer.
628 Stained cells were analyzed with a CytoFLEX flow cytometer (Beckman Coulter) or an LSR II flow cytometer
629 (BD Biosciences). Stained live cells were sorted using FACSAria cell sorters (BD Biosciences) using a 100 μm
630 nozzle and event rate of 3000-4000 per second into collecting vessels kept at 4 °C until downstream use. Gating
631 strategies are found in Supplementary Fig. S9.
632
633 In vitro cellular assays

634 For tumor-T cell co-culture, CD8 T cells and tumor cells were sorted as above. Prior to plating, 96 well
635 flat bottom plate wells were coated with anti-CD3 antibody (clone 145-2C11, 10 μg/mL final in PBS, UCSF
636 Monoclonal Antibody Core) for 4-6 hours at 37°C and washed twice with PBS. For each cell population in the
637 co-culture, 3.5 x 10^4 cells were plated together with anti-CD28 antibody (clone 37.51, 3 μg/mL final, UCSF
638 Monoclonal Antibody Core) and any neutralizing antibodies in 200 μL final volume of T cell media (RPMI 1640
639 with 10% FCS, 25mM HEPES, 2mM L-glutamine, 33μM 2-mercaptoethanol, 100 U mL^{-1} penicillin and 100 μg
640 mL^{-1} streptomycin. After 24 hours of culture in a 37 °C incubator, the supernatant was collected for G-CSF ELISA.
641 For OT-I T cell MDSC assay, neutrophils were sorted as above from LLC MSI-H tumor, while OT-I cells
642 were harvested from spleen of OT-I CD45.1 mice (RRID:IMSR_JAX:003831) by processing over a 70 μm filter.
643 In 96 well U-bottom plates, 1 x 10^5 OT-I splenocytes and 2.5 x 10^4 sorted neutrophils were combined with or
644 without SIINFEKL peptide at 0.4 ng/mL in 200 μL T cell media. Cells were incubated in a 37 °C CO2 incubator
645 for 42 hours, then BrdU was added to the wells at 10 μM final concentration for an additional 6 hours. Cells were
646 collected and stained with Zombie NIR, anti-TCRβ, anti-CD45.1, and anti-CD8a antibodies then anti-BrdU
647 antibody as per manufacturer protocol for the eBioscience BrdU Staining Kit for Flow Cytometry. Cells were
648 analyzed using an LSR II flow cytometer.
649 For assessment of G-CSF and CXCL1 by ELISA following TNFα, IL-1α, or IL1-β stimulation, 10 ng/ml
650 of cytokine (Biolegend) was added (unless otherwise stated) to cell culture media 24 hours prior to collection of
651 supernatant for analysis using ELISA kits for G-CSF (Abcam, ab197743), or CXCL1 (Abcam, ab216951). For
652 analysis of IκBα by flow cytometry, TNFα and IL-1α (1 ng/ml) was added to culture media 20 minutes prior to
653 cell harvest and processing for staining and flow cytometry as above.
654
655 Quantitative reverse transcription PCR
656 Cells were sorted into 500 μL TRIzol reagent (Thermo Fisher Scientific). RNA was isolated using Direct-
657 zol 96 MagBead RNA kit (Zymo) per manufacturer protocol. cDNA was generated using Iscript Reverse
658 Transcription Supermix (Bio-Rad) per manufacturer protocol. Real-time PCR was performed using Taqman

659 primers for *Csf3* (Thermo Fisher Scientific Mm00438334_m1), *Cxcl1* (Mm04207460_m1), *Il1a*
660 (Mm00439620_m1), *Il1b* (Mm00434228_m1) and *Gapdh* (Mm99999915_g1) on a Bio-Rad C1000 Thermal
661 Cycler. ΔΔCq values were calculated against *Gapdh* then against biological control. For breast cancer organoid
662 RT-qPCR, Taqman primers for *IL1R1* (Hs00991010_m1), *TNFRSF1A* (Hs01042313_m1), *CXCL8*
663 (Hs00174103_m1), and *UBC* (Hs05002522_g1) were used.
664
665 Western blot
666 Protein lysates were generated using RIPA buffer containing protease inhibitor (Cell Biolabs) on ice for
667 10 minutes, followed by centrifugation at 14,000 rpm for 10 minutes at 4 °C. Supernatant containing cell lysate
668 was collected, and 20 μg of lysate was loaded onto NuPAGE 4-12% Bis-Tris protein gel (Thermo Fisher
669 Scientific). Gels were run in NuPAGE MOPS SDS running buffer, then transferred to a nitrocellulose blot in
670 NuPAGE Transfer Buffer. Blots were incubated with PBS-T (0.1% Tween 20) with 5% BSA, then incubated with
671 primary antibody against MSH2 (clone FE11, Thermo Fisher Scientific, 1:500 dilution, RRID: AB_2533139)
672 overnight at 4 °C. After washing in PBST, HRP goat anti-mouse IgG secondary antibody (RRID:AB_562588)
673 was added in PBS-T and incubated for 1 hour. Blot was developed using SuperSignal West Pico PLUS
674 chemiluminescent substrate (Thermo Fisher Scientific) and acquired using a Bio-Rad ChemiDoc system.
675
676 Organoid culture
677 Organoid cultures were generated from breast tumor samples collected at Brigham & Women's Hospital and
678 processed on the day of surgery with appropriate informed consent for tissue acquisition for scientific research.
679 Viable tissue was minced and placed in a 50 mL conical tube that contained: 18 mL AdDF+++ (Advanced
680 DMEM/F12 containing Glutamax, HEPES, and antibiotics) + 2 mL collagenase (10 mg/ml). The tube was placed
681 into an orbital shaker at 37 °C for 30 min. After digestion, 30 mL AdDF+++ plus 2% FBS was added to the tube
682 and the pellet was collected, resuspended in BME type 2 (R&D Systems, 353300502), and cultured as previously
683 described[111]. Briefly, a drop of 50 μL of this suspension was placed in the center of a well in a 24-well non-
684 treated culture plate (Corning, 3738) and transferred to a 37°C, 5% CO2 incubator to harden for 20 min.

685 Subsequently, 500 µL Type 1 breast cancer organoid culture medium[112] was added to the well. Medium was
686 changed every 2-3 days. TrypLE Express (Gibco, 12604013) was used for passaging approximately every 1–2
687 weeks. Organoids were viably frozen by Recovery™ Cell Culture Freezing Medium (Gibco, 12648010).
688 TORG40 was generated from a triple-negative inflammatory breast cancer, and TORG139 was generated from a
689 triple-negative breast cancer.
690
691 Human breast cancer single-cell RNAseq analysis
692 Data was obtained from https://lambrechtslab.sites.vib.be/en/single-cell and is deposited at the European
693 Genome-phenome Archive (EGA) under study no (EGAS00001004809) and under data accession
694 no. EGAD00001006608. Data was imported to Seurat (v. 4.1.0) as a Seurat Object. For quality control, the data
695 was previously filtered by excluding all cells expressing <200 or >6,000 genes, cells that contained <400 unique
696 molecular identifiers (UMIs), and cells with >15% mitochondrial counts. Raw counts were normalized using
697 sctransform (v. 0.3.3) and glmGamPoi (v. 1.2.0) with regression of cell cycle genes, percent mitochrondrial counts,
698 and number of UMIs (counts). Principal Component Analysis (PCA) was performed using variable genes. Cell
699 clusters were defined using Seurat's FindNeighbors (dim 1-20) and FindClusters (resolution 0.5) and were
700 visualized using Uniform Manifold Approximation and Projection (UMAP). Cluster annotations for major cell
701 types were provided in the metadata and aligned well with cluster assignment. The T cell cluster was fine
702 annotated into CD4, CD8, and Tregs based on expression of *CD4*, *CD8A*, *CD8B*, and *FOXP3*. The data was then
703 filtered to CD8 T cells, tumor cells, CD4 T cells, and myeloid cells.
704 CD8 T cells were reclustered using the above parameters. Clusters were defined using the FindAllMarkers
705 function in Seurat which identified differentially expressed genes (DEGs). Genes must be expressed in 25% of
706 cells. DEGs between specific clusters, found using FindMarkers, were plotted using EnhancedVolcano (v. 1.8.0).
707 For genes of interest, the density, or for two genes the joint density, was plotted in UMAP space using Nebulosa
708 (v. 1.0.2). DEenrichRPlot (Seurat and enrichR (v. 3.0)) was run to determine GO terms enriched in specific
709 clusters using the GO_Biological_Process_2021 list.

710 The proportion of cells in a given cluster from "Pre" or "On" treatment was calculated on a per patient
711 basis by normalizing for the number of CD8s per patient. The frequency of any cluster of CD8s compared "Pre"
712 vs "On" treatment was normalized to the number of cells in the entire tumor. Paired differences in cluster
713 frequency were tested using paired Wilcoxon. Tumor cell scoring for NF-κB/TNFα signaling was performed
714 using the gene set "HALLMARK_TNFA_SCORING_VIA_NFKB" obtained from Molecular Signatures
715 Database or MSigDB and the AddModuleScore function in Seurat. Differences in score were calculated "Pre" vs
716 "On" treatment.
717
718 CIBERSORTx analysis
719 COAD bulk RNA sequencing data from TCGA was analyzed using the CIBERTSORTx[72] platform
720 (cibersortx.stanford.edu). Proportion of neutrophils as percentage of immune cells in sample was deconvoluted
721 using the LM22 signature matrix and default parameters. MSIsensor[113] scores for each tumor sample was used to
722 stratify patients as MSS or MSI-H using a published dataset[10].
723
724 Human peripheral blood neutrophil to lymphocyte ratio analysis
725 Patients with MSI-H tumors from our institutional database of tumors submitted for next generation
726 sequencing were identified (UCSF IRB 18-24633). Dataset was further filtered to non-central nervous system
727 tumors and patients receiving ICI therapy (included single or combinations of pembrolizumab, nivolumab,
728 atezolizumab, or ipilimumab) during their course of treatment. Among this group of patients, those who
729 experienced radiologist-confirmed imaging-based progression were identified, with the date of progression
730 defined as the date of imaging. 6-week averaged values were derived from all available complete blood count
731 with differential lab testing prior to initiation of immunotherapy or prior to progression of disease. For each patient
732 and timepoint, the absolute neutrophil count was divided by the absolute lymphocyte count to derive the
733 neutrophil to lymphocyte ratio (NLR).
734
735 Human lung cancer dataset analysis

736 Log2 normalized TPM and relevant clinical data were downloaded from EGA (https://ega-
737 archive.org/studies/EGAS00001005013) for the OAK clinical trial[76]. Single sample gene signature scores were
738 assigned to bulk RNA-seq samples from OAK by taking the median z-score of the genes that comprise the
739 signature
740 (*"IL1R1","TNFRSF1A","IL1A","IL1B","TNF","CD69","CXCL1","CXCL2","CXCL8","NFKB1","NFKB2","CS*
741 *F3"*). Patients were grouped into "high" or "low" expression based on the cohort-wide median expression of the
742 signature and also CD8A expression. For resultant survival analyses in the atezolizumab arm of OAK, the log-
743 rank test was used to compare Kaplan-Meier survival curves and cox proportional hazards regression models
744 were used to generate hazard ratios and 95% confidence intervals.
745
746 Statistical analyses
747 Unless otherwise indicated, statistical testing was performed using GraphPad Prism. Prior to significance
748 testing for differences among groups, the normality of data distribution for each group being tested was tested via
749 Shapiro-Wilk test, where data with $p > 0.05$ were considered normally distributed. For normal datasets, t test was
750 performed, with Welch's correction if F test demonstrated unequal SD between groups. For non-normal datasets,
751 Mann-Whitney U test was used. Multiple testing correction was performed using Holm-Sidak method to generate
752 adjusted p values where indicated. Two-tailed tests were performed where direction of change could not be
753 hypothesized a priori, and one tailed-tests were performed to test a specific direction of change. All data points
754 represent biological replicates.
755
756 **Data and reagent availability**
757 Mass cytometry data are deposited into Mendeley Data and also available by request to the senior author
758 without restrictions. Bulk RNA sequencing data and exome sequencing data are deposited into NCBI SRA
759 database. All cell lines are available upon request to the senior author without restrictions.
760
761 **Code availability**

762 R code for analyses performed within the manuscript will be made available upon request.

763

764 **References**

765 1. Sharma, P., Hu-Lieskovan, S., Wargo, J. A. & Ribas, A. Primary, Adaptive, and Acquired Resistance to
766 Cancer Immunotherapy. *Cell* **168**, 707–723 (2017).
767 2. Zhang, L. *et al.* Intratumoral T Cells, Recurrence, and Survival in Epithelial Ovarian Cancer. *New*
768 *England Journal of Medicine* **348**, 203–213 (2003).
769 3. Galon, J. *et al.* Type, density, and location of immune cells within human colorectal tumors predict
770 clinical outcome. *Science (1979)* **313**, 1960–1964 (2006).
771 4. Tumeh, P. C. *et al.* PD-1 blockade induces responses by inhibiting adaptive immune resistance. *Nature*
772 **515**, 568–571 (2014).
773 5. Waldman, A. D., Fritz, J. M. & Lenardo, M. J. A guide to cancer immunotherapy: from T cell basic
774 science to clinical practice. *Nature Reviews Immunology 2020 20:11* **20**, 651–668 (2020).
775 6. Galon, J. & Bruni, D. Approaches to treat immune hot, altered and cold tumours with combination
776 immunotherapies. *Nature Reviews Drug Discovery 2018 18:3* **18**, 197–218 (2019).
777 7. Le, D. T. *et al.* PD-1 Blockade in Tumors with Mismatch-Repair Deficiency. *New England Journal of*
778 *Medicine* **372**, 2509–2520 (2015).
779 8. Le, D. T. *et al.* Mismatch repair deficiency predicts response of solid tumors to PD-1 blockade. *Science*
780 **357**, 409–413 (2017).
781 9. Germano, G. *et al.* Inactivation of DNA repair triggers neoantigen generation and impairs tumour
782 growth. *Nature* **552**, 1–5 (2017).
783 10. Mandal, R. *et al.* Genetic diversity of tumors with mismatch repair deficiency influences anti–PD-1
784 immunotherapy response. *Science (1979)* **364**, 485–491 (2019).
785 11. Petrelli, F., Ghidini, M., Ghidini, A. & Tomasello, G. Outcomes Following Immune Checkpoint Inhibitor
786 Treatment of Patients With Microsatellite Instability-High Cancers: A Systematic Review and Meta-
787 analysis. *JAMA Oncol* **6**, 1068–1071 (2020).
788 12. Li, F. *et al.* The association between CD8+ tumor-infiltrating lymphocytes and the clinical outcome of
789 cancer immunotherapy: A systematic review and meta-analysis. *EClinicalMedicine* **41**, 101134 (2021).
790 13. Kim, T. M., Laird, P. W. & Park, P. J. The landscape of microsatellite instability in colorectal and
791 endometrial cancer genomes. *Cell* **155**, 858 (2013).
792 14. Le, D. T. *et al.* PD-1 Blockade in Tumors with Mismatch-Repair Deficiency. *New England Journal of*
793 *Medicine* **372**, 2509–2520 (2015).
794 15. Le, D. T. *et al.* Mismatch repair deficiency predicts response of solid tumors to PD-1 blockade. *Science*
795 *(1979)* **357**, 409–413 (2017).
796 16. Roudko, V. *et al.* Shared Immunogenic Poly-Epitope Frameshift Mutations in Microsatellite Unstable
797 Tumors. *Cell* **183**, 1634-1649.e17 (2020).
798 17. Marabelle, A. *et al.* Efficacy of Pembrolizumab in Patients With Noncolorectal High Microsatellite
799 Instability/Mismatch Repair–Deficient Cancer: Results From the Phase II KEYNOTE-158 Study.
800 *Journal of Clinical Oncology* **38**, 1–10 (2019).
801 18. Le, D. T. *et al.* Phase II Open-Label Study of Pembrolizumab in Treatment-Refractory, Microsatellite
802 Instability–High/Mismatch Repair–Deficient Metastatic Colorectal Cancer: KEYNOTE-164. *Journal of*
803 *Clinical Oncology* **38**, 11–19 (2019).
804 19. Shalapour, S. & Karin, M. Pas de Deux: Control of Anti-tumor Immunity by Cancer-Associated
805 Inflammation. *Immunity* **51**, 15–26 (2019).
806 20. Giri, D. K. & Aggarwal, B. B. Constitutive Activation of NF-κB Causes Resistance to Apoptosis in
807 Human Cutaneous T Cell Lymphoma HuT-78 Cells: AUTOCRINE ROLE OF TUMOR NECROSIS
808 FACTOR AND REACTIVE OXYGEN INTERMEDIATES *. *Journal of Biological Chemistry* **273**,
809 14008–14014 (1998).

21. Wolf, J. S. *et al.* IL (interleukin)-1alpha promotes nuclear factor-kappaB and AP-1-induced IL-8 expression, cell survival, and proliferation in head and neck squamous cell carcinomas. *Clin Cancer Res* **7**, 1812–1820 (2001).
22. Karin, M. NF-κB as a Critical Link Between Inflammation and Cancer. *Cold Spring Harb Perspect Biol* **1**, a000141 (2009).
23. Xia, Y., Shen, S. & Verma, I. M. NF-κB, an Active Player in Human CancersNF-κB, an Active Player in Human Cancers. *Cancer Immunol Res* **2**, 823–830 (2014).
24. Wang, D. & Du Bois, R. N. Immunosuppression associated with chronic inflammation in the tumor microenvironment. *Carcinogenesis* **36**, 1085–1093 (2015).
25. Greten, F. R. & Grivennikov, S. I. Inflammation and Cancer: Triggers, Mechanisms, and Consequences. *Immunity* **51**, 27–41 (2019).
26. Taniguchi, K. & Karin, M. NF-κB, inflammation, immunity and cancer: coming of age. *Nature Reviews Immunology 2018 18:5* **18**, 309–324 (2018).
27. Tu, S. *et al.* Overexpression of Interleukin-1β Induces Gastric Inflammation and Cancer and Mobilizes Myeloid-Derived Suppressor Cells in Mice. *Cancer Cell* **14**, 408–419 (2008).
28. Yu, J. *et al.* Noncanonical NF-κB Activation Mediates STAT3-Stimulated IDO Upregulation in Myeloid-Derived Suppressor Cells in Breast Cancer. *The Journal of Immunology* **193**, 2574–2586 (2014).
29. Hu, X. *et al.* Transmembrane TNF-α Promotes Suppressive Activities of Myeloid-Derived Suppressor Cells via TNFR2. *The Journal of Immunology* **192**, 1320–1331 (2014).
30. Achyut, B. R. *et al.* Canonical NFκB signaling in myeloid cells is required for the glioblastoma growth. *Sci Rep* **7**, (2017).
31. Li, T. *et al.* c-Rel is a myeloid checkpoint for cancer immunotherapy. *Nature Cancer 2020 1:5* **1**, 507–517 (2020).
32. Grinberg-Bleyer, Y. *et al.* NF-κB c-Rel Is Crucial for the Regulatory T Cell Immune Checkpoint in Cancer. *Cell* **170**, 1096-1108.e13 (2017).
33. Lim, S. O. *et al.* Deubiquitination and Stabilization of PD-L1 by CSN5. *Cancer Cell* **30**, 925–939 (2016).
34. Lu, C. *et al.* p50 suppresses cytotoxic T lymphocyte effector function to regulate tumor immune escape and response to immunotherapy. *J Immunother Cancer* **8**, e001365 (2020).
35. Perez-Ruiz, E. *et al.* Prophylactic TNF blockade uncouples efficacy and toxicity in dual CTLA-4 and PD-1 immunotherapy. *Nature 2019 569:7756* **569**, 428–432 (2019).
36. Bertrand, F. *et al.* TNFα blockade overcomes resistance to anti-PD-1 in experimental melanoma. *Nature Communications 2017 8:1* **8**, 1–13 (2017).
37. Blank, C. U. *et al.* Defining 'T cell exhaustion'. *Nature Reviews Immunology 2019 19:11* **19**, 665–674 (2019).
38. Gabrilovich, D. I. & Nagaraj, S. *Myeloid-Derived Suppressor Cells as Regulators of the Immune System*. *Nature Reviews Immunology* vol. 9 162–174 (Nature Publishing Group, 2009).
39. Nebot-Bral, L. *et al.* Overcoming resistance to αPD-1 of MMR-deficient tumors with high tumor-induced neutrophils levels by combination of αCTLA-4 and αPD-1 blockers. *J Immunother Cancer* **10**, (2022).
40. Westcott, P. M. K. *et al.* Mismatch repair deficiency is not sufficient to elicit tumor immunogenicity. *Nat Genet* **55**, 1686–1695 (2023).
41. Roth, T. L. *et al.* Reprogramming human T cell function and specificity with non-viral genome targeting. *Nature* **13**, 27.
42. Wolf, Y. *et al.* UVB-Induced Tumor Heterogeneity Diminishes Immune Response in Melanoma. *Cell* **179**, 219-235.e21 (2019).
43. Woerner, S. M. *et al.* Detection of coding microsatellite frameshift mutations in DNA mismatch repair-deficient mouse intestinal tumors. *Mol Carcinog* **54**, 1376–1386 (2015).
44. Bjerregaard, A. M., Nielsen, M., Hadrup, S. R., Szallasi, Z. & Eklund, A. C. MuPeXI: prediction of neo-epitopes from tumor sequencing data. *Cancer Immunology, Immunotherapy* **66**, 1123–1130 (2017).
45. Sari, G. & Rock, K. L. Tumor immune evasion through loss of MHC class-I antigen presentation. *Curr Opin Immunol* **83**, 102329 (2023).

860 46. McInnes, L., Healy, J., Saul, N. & Großberger, L. UMAP: Uniform Manifold Approximation and
861 Projection. *J Open Source Softw* **3**, 861 (2018).
862 47. Zhao, J. *et al.* Detection of differentially abundant cell subpopulations in scRNA-seq data. *Proceedings*
863 *of the National Academy of Sciences* **118**, e2100293118 (2021).
864 48. Kurtulus, S. *et al.* Checkpoint Blockade Immunotherapy Induces Dynamic Changes in PD-1−CD8+
865 Tumor-Infiltrating T Cells. *Immunity* **50**, 181-194.e6 (2019).
866 49. Allen, B. M. *et al.* Systemic dysfunction and plasticity of the immune macroenvironment in cancer
867 models. *Nat Med* **26**, 1125–1134 (2020).
868 50. Veglia, F., Sanseviero, E. & Gabrilovich, D. I. Myeloid-derived suppressor cells in the era of increasing
869 myeloid cell diversity. *Nature Reviews Immunology* 1–14 Preprint at https://doi.org/10.1038/s41577-020-
870 00490-y (2021).
871 51. Waight, J. D., Hu, Q., Miller, A., Liu, S. & Abrams, S. I. Tumor-Derived G-CSF Facilitates Neoplastic
872 Growth through a Granulocytic Myeloid-Derived Suppressor Cell-Dependent Mechanism. *PLoS One* **6**,
873 e27690 (2011).
874 52. Chakraborty, A. & Guha, S. Granulocyte Colony-Stimulating Factor/Granulocyte Colony-Stimulating
875 Factor Receptor Biological Axis Promotes Survival and Growth of Bladder Cancer Cells. *Urology* **69**,
876 1210–1215 (2007).
877 53. Tsukuda, M. *et al.* A tumor cell line producing granulocyte colony-stimulating factor and an immune
878 suppressive factor. *Biotherapy 1993 6:3* **6**, 217–223 (1993).
879 54. Yuan, M. *et al.* Tumor-derived CXCL1 promotes lung cancer growth via recruitment of tumor-associated
880 Neutrophils. *J Immunol Res* **2016**, (2016).
881 55. Caldwell, J. & Emerson, S. G. IL-1α and TNFα act synergistically to stimulate production of myeloid
882 colony-stimulating factors by cultured human bone marrow stromal cells and cloned stromal cell strains.
883 *J Cell Physiol* **159**, 221–228 (1994).
884 56. Caldwell, J. & Emerson, S. G. Interleukin-1 alpha upregulates tumor necrosis factor receptors expressed
885 by a human bone marrow stromal cell strain: implications for cytokine redundancy and synergy. *Blood*
886 **86**, 3364–3372 (1995).
887 57. Bianchi, A. *et al.* Cell-Autonomous Cxcl1 Sustains Tolerogenic Circuitries and Stromal Inflammation via
888 Neutrophil-Derived TNF in Pancreatic Cancer. *Cancer Discov* **13**, 1428–1453 (2023).
889 58. Boraschi, D. *et al.* Endothelial Cells Express the Interleukin-1 Receptor Type I. *Blood* **78**, 1262–1267
890 (1991).
891 59. Tartey, S., Neale, G., Vogel, P., Malireddi, R. K. S. & Kanneganti, T.-D. A MyD88/IL1R Axis Regulates
892 PD-1 Expression on Tumor-Associated Macrophages and Sustains Their Immunosuppressive Function in
893 Melanoma. *Cancer Res* **81**, 2358–2372 (2021).
894 60. Keir, M. E., Butte, M. J., Freeman, G. J. & Sharpe, A. H. PD-1 and Its Ligands in Tolerance and
895 Immunity. *Annu Rev Immunol* **26**, 677–704 (2008).
896 61. Grivennikov, S. I. *et al.* Distinct and Nonredundant In Vivo Functions of TNF Produced by T Cells and
897 Macrophages/Neutrophils: Protective and Deleterious Effects. *Immunity* **22**, 93–104 (2005).
898 62. Bassez, A. *et al.* A single-cell map of intratumoral changes during anti-PD1 treatment of patients with
899 breast cancer. *Nat Med* **27**, 820–832 (2021).
900 63. Cibrián, D. & Sánchez-Madrid, F. CD69: from activation marker to metabolic gatekeeper. *Eur J*
901 *Immunol* **47**, 946–953 (2017).
902 64. Reed, J. C., Alpers, J. D., Nowell, P. C. & Hoover, R. G. Sequential expression of protooncogenes during
903 lectin-stimulated mitogenesis of normal human lymphocytes. *Proceedings of the National Academy of*
904 *Sciences* **83**, 3982–3986 (1986).
905 65. Sun, F. *et al.* The MAPK dual specific phosphatase (DUSP) proteins: A versatile wrestler in T cell
906 functionality. *Int Immunopharmacol* **98**, 107906 (2021).
907 66. Galeano Niño, J. L. *et al.* Cytotoxic T cells swarm by homotypic chemokine signalling. *Elife* **9**, e56554
908 (2020).
909 67. Liberzon, A. *et al.* The Molecular Signatures Database Hallmark Gene Set Collection. *Cell Syst* **1**, 417–
910 425 (2015).

68. Grieshaber-Bouyer, R. *et al.* The neutrotime transcriptional signature defines a single continuum of neutrophils across biological compartments. *Nat Commun* **12**, 2856 (2021).
69. Pelka, K. *et al.* Multicellular immune hubs and their organization in MMRd and MMRp colorectal cancer. *bioRxiv* 2021.01.30.426796 (2021) doi:10.1101/2021.01.30.426796.
70. Dolcetti, R. *et al.* High Prevalence of Activated Intraepithelial Cytotoxic T Lymphocytes and Increased Neoplastic Cell Apoptosis in Colorectal Carcinomas with Microsatellite Instability. *Am J Pathol* **154**, 1805–1813 (1999).
71. Phillips, S. M. *et al.* Tumour-infiltrating lymphocytes in colorectal cancer with microsatellite instability are activated and cytotoxic. *British Journal of Surgery* **91**, 469–475 (2004).
72. Newman, A. M. *et al.* Determining cell type abundance and expression from bulk tissues with digital cytometry. *Nat Biotechnol* **37**, 773–782 (2019).
73. Howard, R., Kanetsky, P. A. & Egan, K. M. Exploring the prognostic value of the neutrophil-to-lymphocyte ratio in cancer. *Sci Rep* **9**, 19673 (2019).
74. Nebot-Bral, L. *et al.* Overcoming resistance to αPD-1 of MMR-deficient tumors with high tumor-induced neutrophils levels by combination of αCTLA-4 and αPD-1 blockers. *J Immunother Cancer* **10**, e005059 (2022).
75. Fehrenbacher, L. *et al.* Updated Efficacy Analysis Including Secondary Population Results for OAK: A Randomized Phase III Study of Atezolizumab versus Docetaxel in Patients with Previously Treated Advanced Non–Small Cell Lung Cancer. *Journal of Thoracic Oncology* **13**, 1156–1170 (2018).
76. Patil, N. S. *et al.* Intratumoral plasma cells predict outcomes to PD-L1 blockade in non-small cell lung cancer. *Cancer Cell* **40**, 289-300.e4 (2022).
77. Betzler, A. C. *et al.* NF-κB and Its Role in Checkpoint Control. *International Journal of Molecular Sciences 2020, Vol. 21, Page 3949* **21**, 3949 (2020).
78. Lalle, G., Twardowski, J. & Grinberg-bleyer, Y. NF-κB in Cancer Immunity: Friend or Foe? *Cells 2021, Vol. 10, Page 355* **10**, 355 (2021).
79. Olivera, I. *et al.* A Therapeutically Actionable Protumoral Axis of Cytokines Involving IL-8, TNFα, and IL-1β. *Cancer Discov* **12**, 2140–2157 (2022).
80. Vignali, D. A. A., Collison, L. W. & Workman, C. J. How regulatory T cells work. *Nature Reviews Immunology 2008 8:7* **8**, 523–532 (2008).
81. Dmitrieva-Posocco, O. *et al.* Cell-Type-Specific Responses to Interleukin-1 Control Microbial Invasion and Tumor-Elicited Inflammation in Colorectal Cancer. *Immunity* **50**, 166-180.e7 (2019).
82. Coffelt, S. B. *et al.* IL-17-producing γδ T cells and neutrophils conspire to promote breast cancer metastasis. *Nature 2015 522:7556* **522**, 345–348 (2015).
83. Roberts, S. J. *et al.* Characterizing tumor-promoting T cells in chemically induced cutaneous carcinogenesis. *Proceedings of the National Academy of Sciences* **104**, 6770–6775 (2007).
84. Kwong, B. Y. *et al.* Molecular Analysis of Tumor-Promoting CD8+ T Cells in Two-Stage Cutaneous Chemical Carcinogenesis. *Journal of Investigative Dermatology* **130**, 1726–1736 (2010).
85. Jain, A. *et al.* T cells instruct myeloid cells to produce inflammasome-independent IL-1β and cause autoimmunity. *Nature Immunology 2019 21:1* **21**, 65–74 (2019).
86. Yogev, N. *et al.* CD4+ T-cell-derived IL-10 promotes CNS inflammation in mice by sustaining effector T cell survival. *Cell Rep* **38**, 110565 (2022).
87. Koncina, E. *et al.* IL1R1+ cancer-associated fibroblasts drive tumor development and immunosuppression in colorectal cancer. *Nat Commun* **14**, 4251 (2023).
88. Bunt, S. K. *et al.* Reduced Inflammation in the Tumor Microenvironment Delays the Accumulation of Myeloid-Derived Suppressor Cells and Limits Tumor Progression. *Cancer Res* **67**, 10019–10026 (2007).
89. Bertrand, F. *et al.* Blocking Tumor Necrosis Factor α Enhances CD8 T-cell–Dependent Immunity in Experimental Melanoma. *Cancer Res* **75**, 2619–2628 (2015).
90. Otano, I. *et al.* Human CD8 T cells are susceptible to TNF-mediated activation-induced cell death. *Theranostics* **10**, 4481–4489 (2020).
91. Landsberg, J. *et al.* Melanomas resist T-cell therapy through inflammation-induced reversible dedifferentiation. *Nature* **490**, 412–416 (2012).

962 92. Govindaraj, C. *et al.* Impaired Th1 immunity in ovarian cancer patients is mediated by TNFR2+ Tregs
963 within the tumor microenvironment. *Clinical Immunology* **149**, 97–110 (2013).
964 93. Tian, J. *et al.* Genomic characteristics and prognosis of lung cancer patients with MSI-H: A cohort study.
965 *Lung Cancer* **181**, 107255 (2023).
966 94. Lu, C. *et al.* DNA Sensing in Mismatch Repair-Deficient Tumor Cells Is Essential for Anti-tumor
967 Immunity. *Cancer Cell* **39**, 96-108.e6.
968 95. Guan, J. *et al.* MLH1 Deficiency-Triggered DNA Hyperexcision by Exonuclease 1 Activates the cGAS-
969 STING Pathway. *Cancer Cell* **39**, (2020).
970 96. McGrail, D. J. *et al.* High tumor mutation burden fails to predict immune checkpoint blockade response
971 across all cancer types. *Annals of Oncology* **32**, 661–672 (2021).
972 97. Paz-Ares, L. *et al.* Canakinumab in combination with docetaxel compared with docetaxel alone for the
973 treatment of advanced non-small cell lung cancer following platinum-based doublet chemotherapy and
974 immunotherapy (CANOPY-2): A multicenter, randomized, double-blind, phase 3 trial. *Lung Cancer* **189**,
975 (2024).
976 98. Tan, D. S. W. *et al.* Canakinumab Versus Placebo in Combination With First-Line Pembrolizumab Plus
977 Chemotherapy for Advanced Non–Small-Cell Lung Cancer: Results From the CANOPY-1 Trial. *Journal
978 of Clinical Oncology* **42**, 192–204 (2023).
979 99. Garon, E. B. *et al.* Canakinumab as Adjuvant Therapy in Patients With Completely Resected Non–Small-
980 Cell Lung Cancer: Results From the CANOPY-A Double-Blind, Randomized Clinical Trial. *Journal of
981 Clinical Oncology* **42**, 180–191 (2023).
982 100. Ridker, P. M. *et al.* Effect of interleukin-1β inhibition with canakinumab on incident lung cancer in
983 patients with atherosclerosis: exploratory results from a randomised, double-blind, placebo-controlled
984 trial. *The Lancet* **390**, 1833–1842 (2017).
985 101. Montfort, A. *et al.* Combining Nivolumab and Ipilimumab with Infliximab or Certolizumab in Patients
986 with Advanced Melanoma: First Results of a Phase Ib Clinical Trial. *Clinical Cancer Research* **27**,
987 1037–1047 (2021).
988 102. Stewart, T. J. & Abrams, S. I. Altered Immune Function during Long-Term Host-Tumor Interactions Can
989 Be Modulated to Retard Autochthonous Neoplastic Growth1. *The Journal of Immunology* **179**, 2851–
990 2859 (2007).
991 103. Xu, B.-L. *et al.* In vivo growth of subclones derived from Lewis lung carcinoma is determined by the
992 tumor microenvironment. *Am J Cancer Res* **12**, (2022).
993 104. Agalioti, T. *et al.* Mutant KRAS promotes malignant pleural effusion formation. *Nat Commun* **8**, 15205
994 (2017).
995 105. Kim, S. *et al.* Strelka2: fast and accurate calling of germline and somatic variants. *Nat Methods* **15**, 591–
996 594 (2018).
997 106. Bray, N. L., Pimentel, H., Melsted, P. & Pachter, L. Near-optimal probabilistic RNA-seq quantification.
998 *Nat Biotechnol* **34**, 525–527 (2016).
999 107. Zunder, E. R. *et al.* Palladium-based mass tag cell barcoding with a doublet-filtering scheme and single-
1000 cell deconvolution algorithm. *Nature Protocols 2014 10:2* **10**, 316–333 (2015).
1001 108. Levine, J. H. *et al.* Data-Driven Phenotypic Dissection of AML Reveals Progenitor-like Cells that
1002 Correlate with Prognosis. *Cell* **162**, 184–197 (2015).
1003 109. Lê, S., Josse, J. & Husson, F. FactoMineR: An R Package for Multivariate Analysis. *J Stat Softw* **25**, 1–
1004 18 (2008).
1005 110. Zheng, S. *et al.* SynergyFinder Plus: Toward Better Interpretation and Annotation of Drug Combination
1006 Screening Datasets. *Genomics Proteomics Bioinformatics* **20**, 587–596 (2022).
1007 111. Rosenbluth, J. M. *et al.* Organoid cultures from normal and cancer-prone human breast tissues preserve
1008 complex epithelial lineages. *Nat Commun* **11**, 1711 (2020).
1009 112. Dekkers, J. F. *et al.* Long-term culture, genetic manipulation and xenotransplantation of human normal
1010 and breast cancer organoids. *Nat Protoc* **16**, 1936–1965 (2021).
1011 113. Niu, B. *et al.* MSIsensor: microsatellite instability detection using paired tumor-normal sequence data.
1012 *Bioinformatics* **30**, 1015–1016 (2014).

Acknowledgements

We thank the UCSF Flow Cytometry Core and S. Tamaki for CyTOF maintenance. We thank E. Engleman and J. Bluestone for cell lines. We thank A. Marson and T. Roth for CRISPR-Cas9 reagents, protocols and equipment. We thank the UCSF Clinical Cancer Genomics Laboratory, Molecular Oncology Initiative, and D. Raleigh for access to the UCSF cBioPortal dataset. This study makes use of publicly available data generated by the Lambrechts group in the BioKey study. A full list of investigators who contributed to the generation of the data, and the funding source is available at doi: 10.1038/s41591-021-01323-8/. The Lambrechts group is not responsible for the analysis or interpretation of the data presented. This study was supported by NIH grants DP5 OD023056 and R01 DE032033 to M.H.S., the UCSF Prostate Cancer Program Pilot Award to N.W.C., and NIH S10 OD018040 to procure the CyTOF mass cytometer. N.W.C. is supported by NIH grant T32 5T32AI007334-33, and ASTRO/ACS Clinician Scientist Development Grant ASTRO-CSDG-23-1036400-01-IBCD. S.M.G. is supported by NIH grants F31CA271748, T32GM1365471, and T32GM00856825, and the UCSF ImmunoX Computational Biology Initiative. K.J.H-G is supported by the Stanford Propel Postdoctoral Scholarship. R.D. is supported by NIH grant F31 CA265128. J.L.Y. is supported by an NSF GRFP fellowship. M.H.S. is an Investigator of the Parker Institute for Cancer Immunotherapy and of the Chan Zuckerberg Biohub. Breast organoid work by J.Z.Y., F.L., D.A.D., and J.M.R. was supported by METAvivor and the Dana-Farber/Harvard Cancer Center Breast SPORE 1P50CA168504.

Contributions

Conceptualization: N.W.C., S.M.G., and M.H.S.; experimental methodology: N.W.C., K.J.H-G., R.D., J.L.Y., N.A.A., I.T., J.Z.Y., F.L., D.A.D., J.M.R.; computational methodology: N.W.C., S.M.G., E.J.K., K.J.H-G., B.Y.N., M.H.S., investigation: all authors; writing, original draft: N.W.C., S.M.G.; writing, review and editing: all authors; funding acquisition: M.H.S. and N.W.C.; supervision: M.H.S.

Figure 1

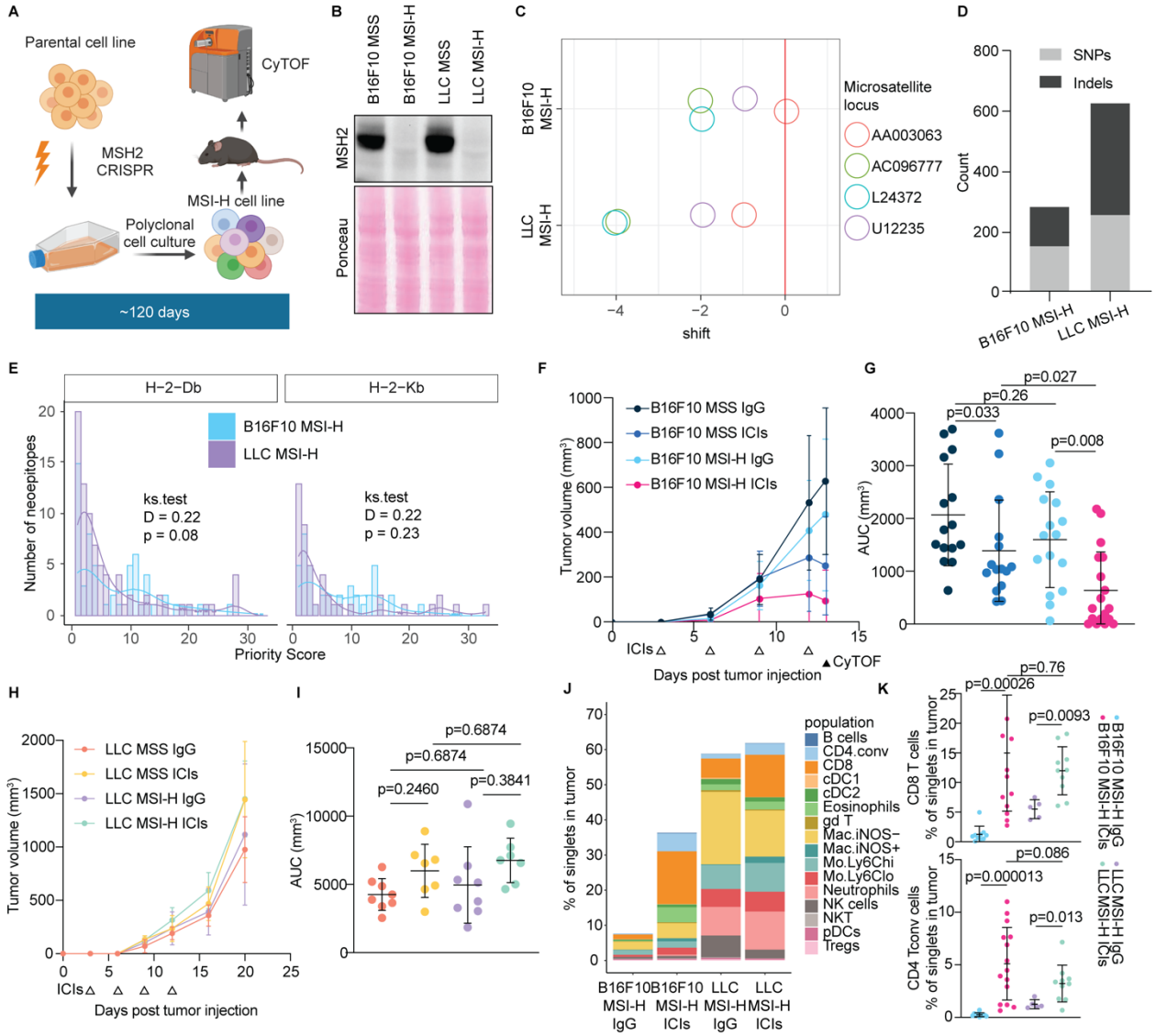

1038

1039 **Figure 1: T cell-infiltrated tumors demonstrate variable responses to ICIs.**

1040 **A,** Outline for generation and experimentation of MSI-H syngeneic tumors. **B,** Representative western blot of
1041 whole cell lysates of indicated cell lines. 3 independent experiments were performed. **C,** Targeted microsatellite
1042 PCR assay comparing amplicon size at indicated loci for MSI-H vs. MSS cell line. Representative of two
1043 independent experiments. **D,** Whole exome sequencing quantification of single nucleotide polymorphisms (SNPs)
1044 and insertion-deletion mutations (indels) for indicated MSI-H cell lines compared to the MSS lines. **E,** MuPeXI
1045 neoepitope affinity scores for indicated cell lines and HLA class. D statistic and p values are calculated using a
1046 two-sided Kolmogorov-Smirnov test. **F and G,** Quantification of mean volumes and area under curves (AUC)
1047 for B16F10 subcutaneous tumors treated with or without anti-PD1 and anti-CTLA4 antibodies (ICIs) at the
1048 indicated timepoints (white arrowhead). Black arrowhead denotes timepoint for sample collection for CyTOF
1049 analysis. n=15-18 mice per condition from two independent experiments. Two-tailed adjusted p value by Mann-
1050 Whitney tests. **H and I,** Analysis as in **(F)** and **(G)** for subcutaneous LLC tumors. n=7-8 mice per condition from
1051 one experiment. Two-tailed adjusted p values by Welch's t tests. **J,** Immune subsets in tumor were defined by
1052 manual gating of CyTOF data from B16F10 subcutaneous or LLC MFP tumors harvested at day 13 post
1053 implantation. Conv=conventional; Mac=macrophages; Mo=monocytes. Bar height for each population represents
1054 the mean of biological replicates (n=5-15 mice) from three independent experiments. **K,** Quantification of CD8
1055 (top panel) and CD4 Tconv (bottom panel) infiltration from **(J)**. Two-tailed adjusted p value by Mann-Whitney
1056 tests. For all applicable panels, error bars represent mean +/- SD.

Figure 2

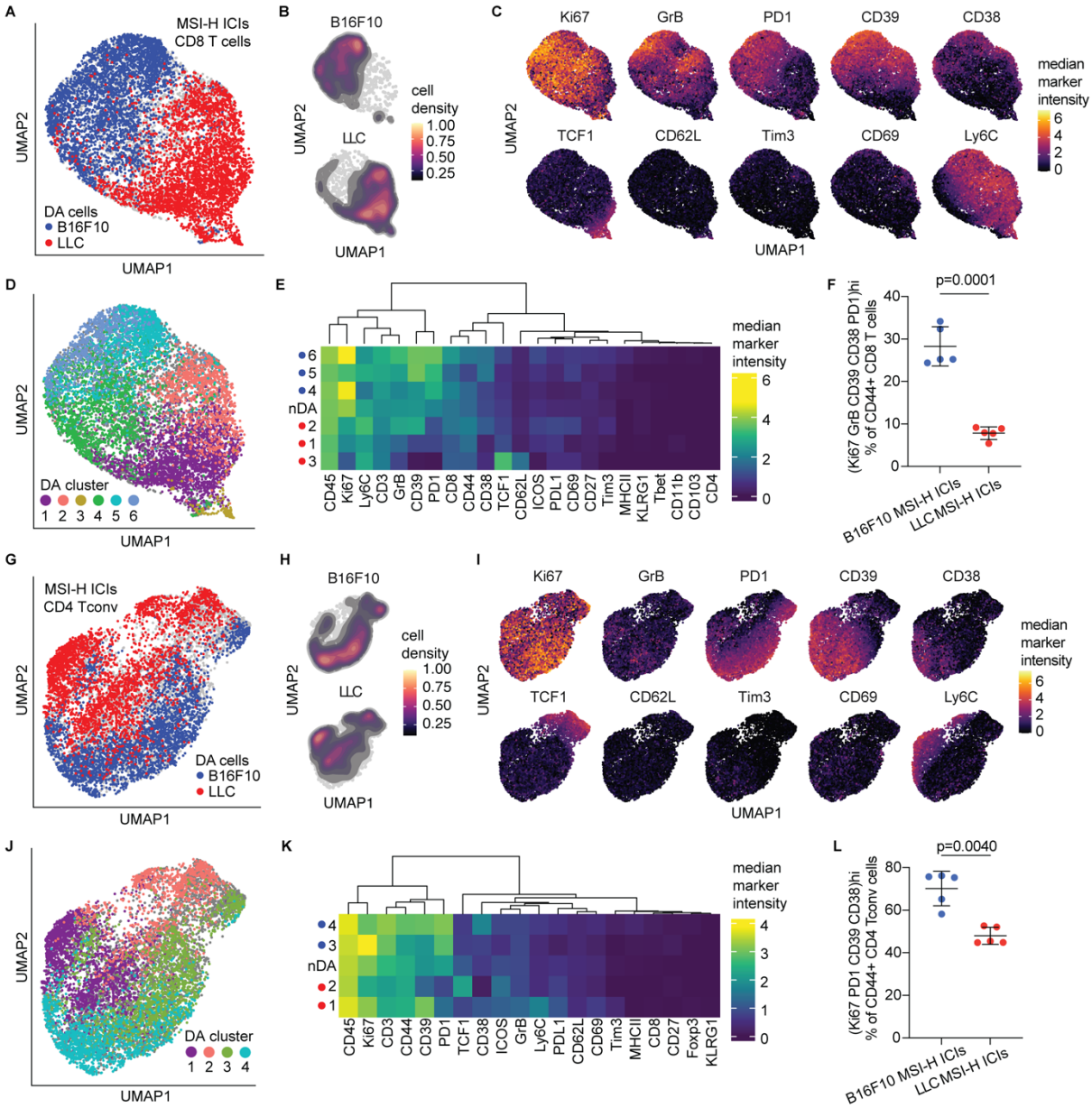

1057

1058 **Figure. 2: Distinct effector marker expression in T cells in ICI-responsive vs. ICI-resistant tumors.**

1059 **A,** Differential abundance (DA) analysis of 10,000 CD44+ CD8 T cells from ICI-treated B16F10 MSI-H and
1060 LLC MSI-H tumors harvested at day 13. CyTOF data acquired with n=5 mice each from one representative
1061 experiment of three independent *in vivo* tumor growth experiments. **B,** Density plots for cells in each tumor type
1062 from **(A). C,** Feature plots for selected markers colored by asinh transformed staining intensity. **D,** Clustering of
1063 DA cells from **(A)** into unsupervised cell subsets. **E,** Heatmap of median marker intensities for cells in each DA
1064 cluster. nDA, non-DA cells. Colored dots indicate clusters more abundant in B16F10 (blue) or LLC (red) tumors.
1065 **F,** Manually gated CD8 T cell subset quantified for B16F10 and LLC tumors. P value by one-tailed Mann-
1066 Whitney test. **G,** DA analysis as in **(A)** for CD44+ CD4 Tconv cells. **H,** Density plots for cells in each tumor type.
1067 **I,** Feature plots for selected markers colored by asinh transformed staining intensity. **J,** Clustering of DA cells
1068 from **(G)** into unsupervised cell subsets. **K,** Heatmap of median marker intensities for cells in each DA cluster.
1069 Colored dots indicate clusters more abundant in B16F10 (blue) or LLC (red) tumors. **L,** Manually gated CD4
1070 Tconv cell subset quantified for B16F10 and LLC tumors. P value by one-tailed Mann-Whitney test. For all
1071 applicable panels, error bars represent mean +/- SD.

Figure 3

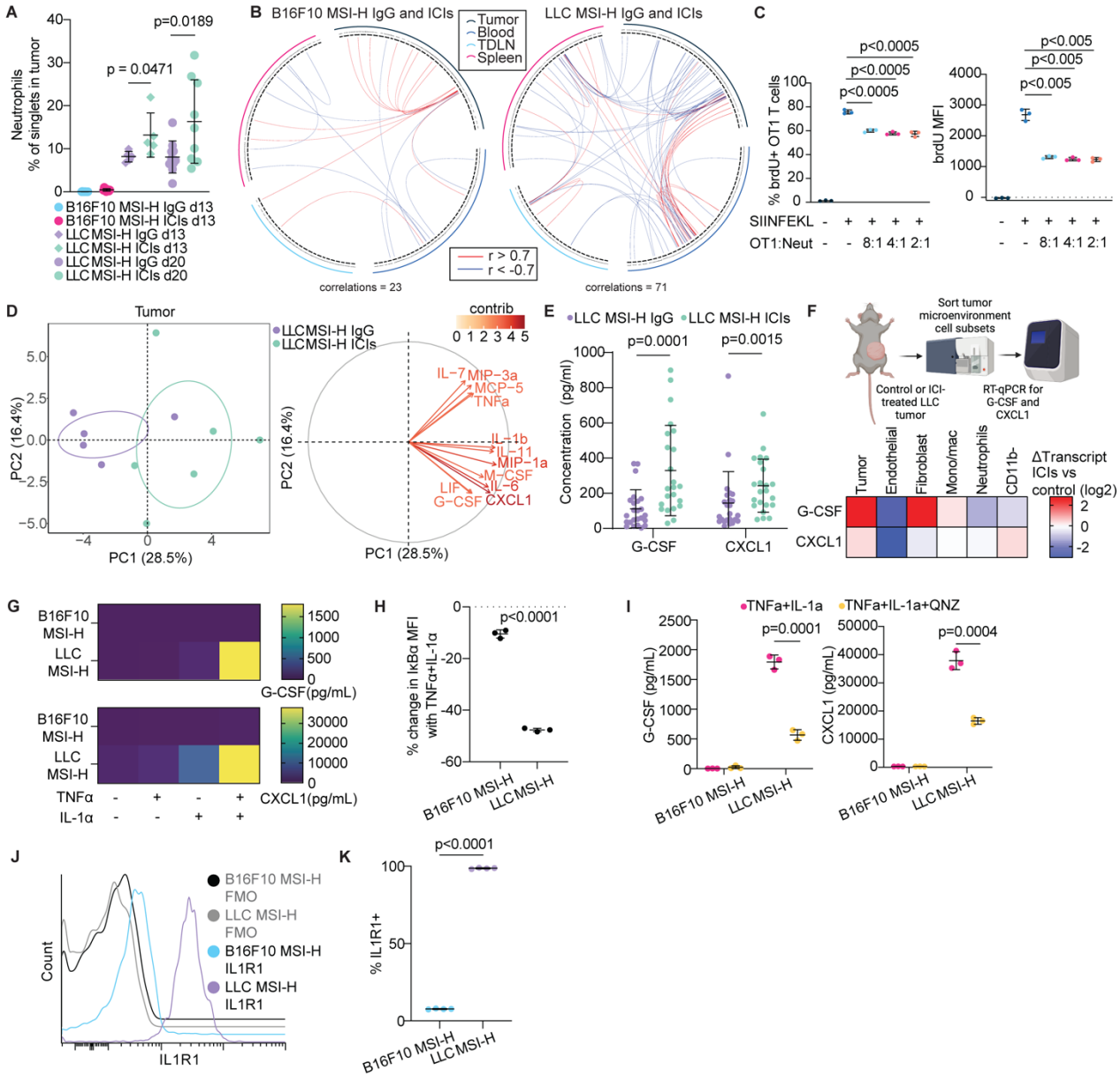

1072

1073 **Figure 3: IL-1 and TNFα synergistically drive immunosuppressive neutrophil inflammation from IL1R1-**
1074 **expressing tumor cells.**
1075 **A,** Quantification of neutrophils in B16F10 and LLC tumors at indicated timepoints and treatment conditions
1076 (n=5-10 mice) from two independent experiments. P values by one-tailed Welch's t test. **B,** Pairwise Spearman
1077 correlation analysis of all unsupervised immune cell clusters across tumor, peripheral blood, tumor-draining
1078 lymph node, and spleen from CyTOF analysis of one representative experiment. Connecting lines indicate pairs
1079 of correlated clusters of which at least one cluster is a neutrophil, indicating positively (red) or negatively (blue)
1080 correlated pairs of clusters with r >0.7 or r <-0.7. Samples harvested at day 13 from n=20 mice for B16F10, and
1081 at day 20 from n=10 mice for LLC. **C,** brdU median fluorescence intensity (MFI) and % positive cell subset
1082 quantification for splenic OT-I T cells cultured with SIINFEKL peptide and/or sorted neutrophils from day 20
1083 LLC MSI-H tumors, from n=3 mice per condition in one experiment. Adjusted p values by Welch's t tests. **D,**
1084 Left panel, principal component (PC) analysis of cytokines in day 20 tumor lysates detected by multiplexed bead
1085 assay in one representative experiment, n=5 per condition. 95% confidence ellipse is shown. Right panel, loadings
1086 plot of contribution by the top 12 cytokines. **E,** Quantification of indicated cytokines in day 20 tumor lysates by
1087 multiplexed bead assay in 5 independent experiments. Two-tailed p values by Mann-Whitney test. **F,** RT-qPCR
1088 of cytokine transcripts from sorted cells from day 20 LLC MSI-H ICI treated tumors, with expression normalized
1089 to control treated tumors. Values represent mean of n=3-6 biological replicates from two independent experiments.
1090 **G,** ELISA quantification of G-CSF in cell culture supernatant of indicated cell lines treated with or without
1091 indicated cytokines for 24h, in one representative experiment with three biological replicates. 5 independent
1092 experiments were performed. **H,** Quantification of IκBα median fluorescence intensity of indicated cell lines with
1093 or without addition TNFα and IL-1α, in one representative experiment with three biological replicates. Two
1094 independent experiments were performed. P value by two-tailed t test. **I,** ELISA quantification of G-CSF and
1095 CXCL1 in cell culture supernatant of indicated cell lines following indicated treatment conditions from one
1096 representative experiment with three biological replicates. Two independent experiments were performed. P value
1097 by two-tailed t test. **J,** Representative histogram of IL1R1 fluorescence staining intensity for indicated cell lines

1098 in comparison to fluorescence-minus-one controls. **K,** Quantification of % IL1R1+ population in indicated cell
1099 lines from one representative experiment with four biological replicates. Two independent experiments were
1100 performed. P value by two-tailed t test. For all applicable panels, error bars represent mean +/- SD.

Figure 4

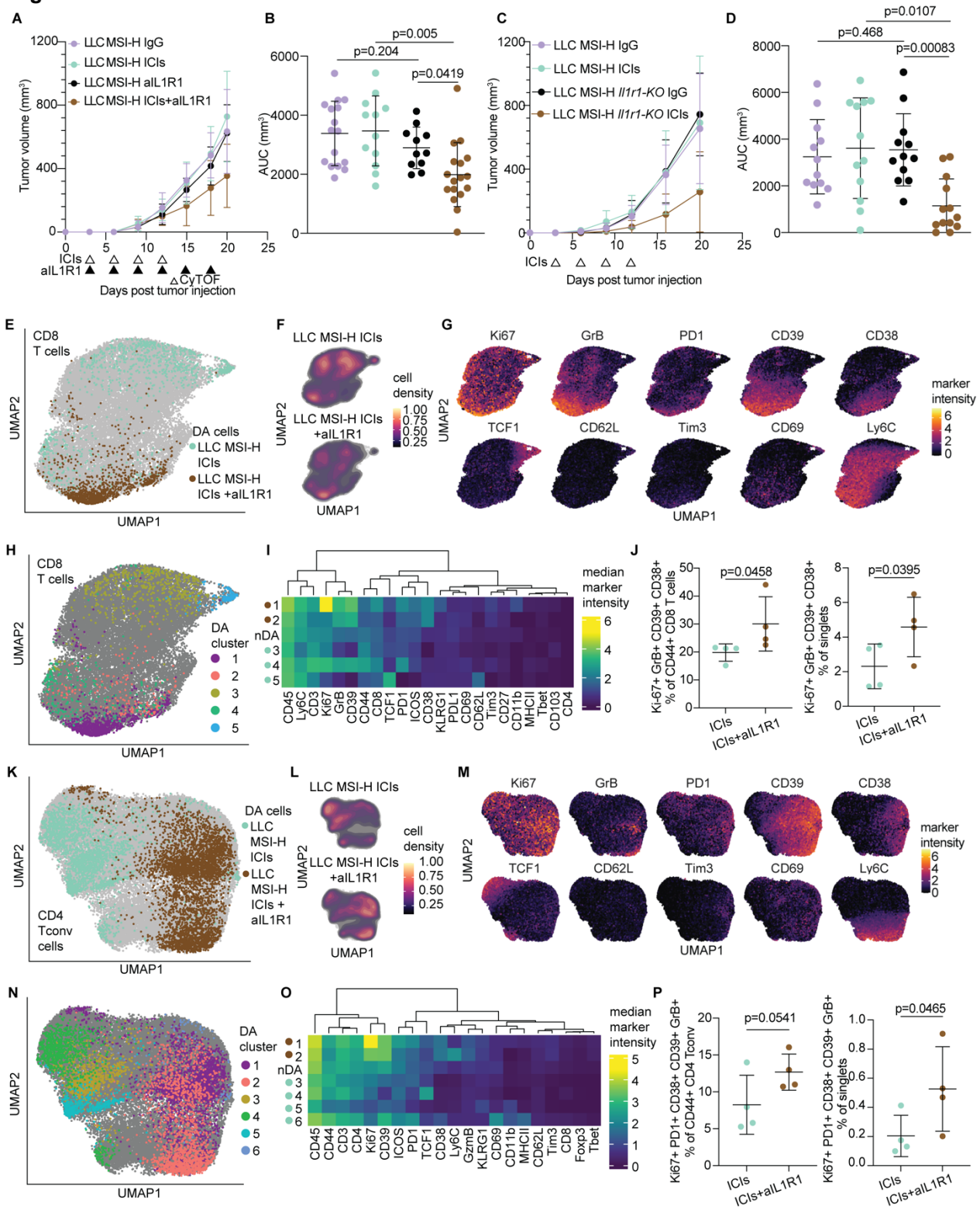

1101

1102 **Figure 4: IL1R1 perturbation limits immunosuppressive inflammation to sensitize resistant tumors to ICIs.**
1103 **A and B,** Quantification of mean volumes and area under curve (AUC) for LLC MSI-H tumors treated with or
1104 without ICIs and IL1R1-neutralizing antibody treatment at the indicated timepoints (arrowheads). n=11-17 mice
1105 per condition from three independent experiments. Two-tailed adjusted p value by Mann-Whitney test. **C and D,**
1106 Quantification of mean volumes and AUCs for LLC MSI-H tumors with or without tumor *Il1r1* knock out (*Il1r1*-
1107 KO) treated with or without ICIs. n=12-13 mice per condition from two independent experiments. Two-tailed
1108 adjusted p value by Mann-Whitney test. **E,** Differential abundance (DA) analysis of 26,400 CD44+ CD8 T cells
1109 from ICI-treated LLC MSI-H tumors +/- aIL1R1 treatment (n=4 mice each from one representative experiment
1110 analyzed by CyTOF) harvested at day 13. Colored dots indicate thresholded top DA cells increased in the
1111 indicated condition. **F,** Density plots for cells in each condition. **G,** Feature plots for selected markers colored by
1112 asinh transformed staining intensity. **H,** Clustering of DA cells from **(E)** into unsupervised cell subsets. **I,**
1113 Heatmap of median marker intensities for cells in each DA cluster. nDA, non-DA cells. Colored dots indicate
1114 clusters enriched in the aIL1R1 condition (brown) vs. control (teal). **J,** Manually gated CD8 T cell subset
1115 quantified for each condition, quantified as % of parental (left panel) and of singlets in tumor (right panel). P
1116 value by one-tailed t test. **K,** DA analysis as in **(E)** for CD44+ CD4 Tconv cells. **L,** Density plots for cells in each
1117 condition. **M,** Feature plots for selected markers colored by asinh transformed staining intensity. **N,** Clustering of
1118 DA cells from **(K)** into unsupervised cell subsets. **O,** Heatmap of median marker intensities for cells in each DA
1119 cluster. nDA, non-DA cells. Colored dots indicate clusters enriched in the aIL1R1 condition (brown) vs. control
1120 (teal). **P,** Manually gated CD4 Tconv cell subset quantified for each condition, quantified as % of parental (left
1121 panel) and of singlets in tumor (right panel). P value by one-tailed t test. For all applicable panels, error bars
1122 represent mean +/- SD.

Figure 5

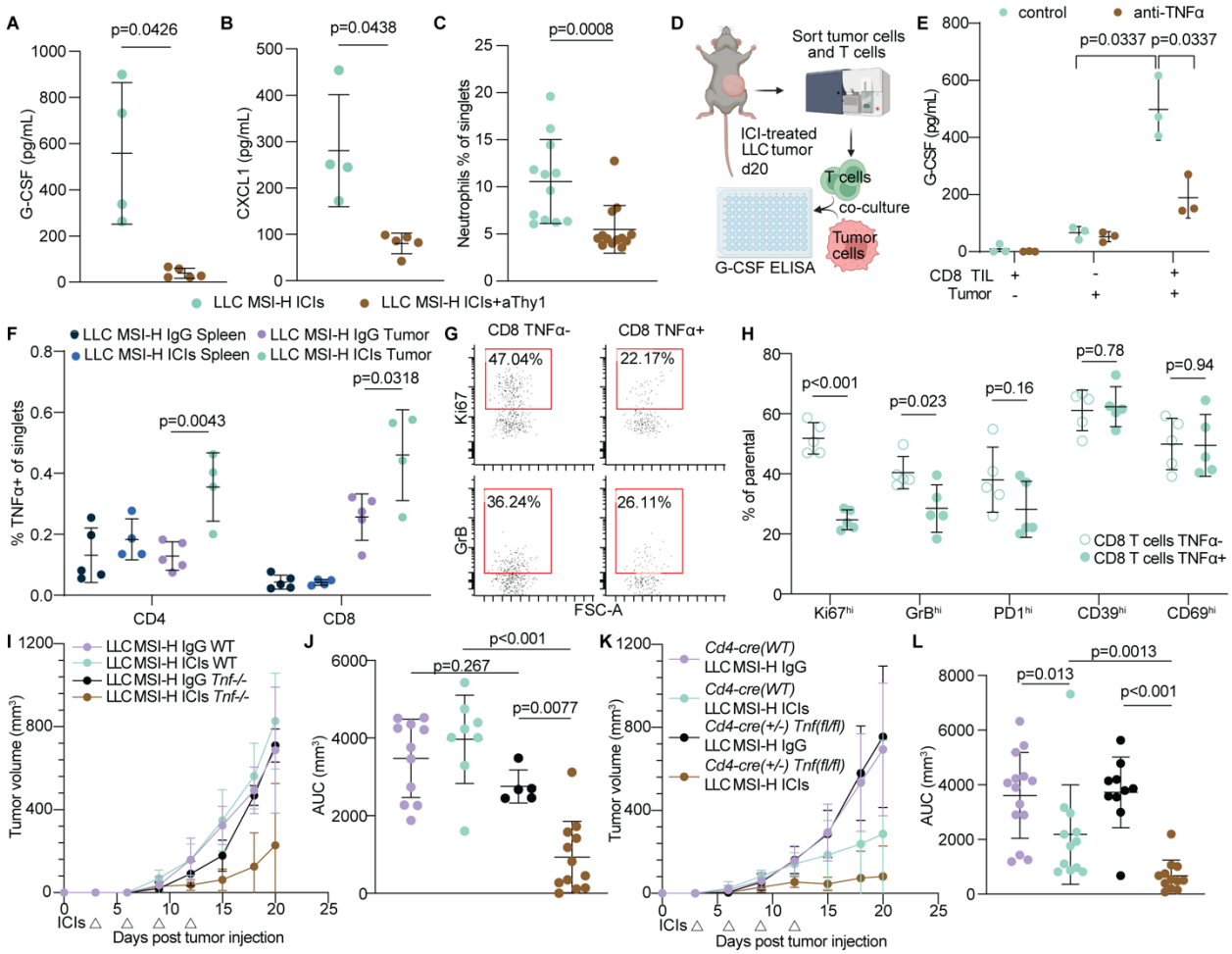

1123

1124 **Figure 5: T cells drive the inflammatory ICI resistance circuit via TNFα.**

1125 **A,** Quantification of G-CSF concentration in day 20 tumor lysates for indicated treatment conditions with n=4-5
1126 mice from one experiment. P value by two-tailed Welch's t test. **B,** Quantification as in (**A**) for CXCL1. **C,**
1127 Quantification of neutrophils in day 20 tumors for indicated treatment conditions in two independent experiments,
1128 n=12-13 mice. P value by two-tailed Welch's t test. **D,** Experimental schematic for T cell-tumor coculture. **E,**
1129 Quantification of G-CSF concentration in supernatant of 24h culture containing indicated sorted cell types from
1130 day 20 LLC MSI-H tumors, with or without TNFα neutralizing antibody, from one representative experiment
1131 with n=3 mice. Two independent experiments were performed. Adjusted p values by two-tailed Welch's t test. **F,**
1132 Quantification of TNFα+ CD4 or CD8 T cells in tumor or spleen of day 20 LLC MSI-H tumor bearing mice
1133 treated with indicated antibodies, n=4-5 mice from one representative experiment. Three independent experiments
1134 were performed. P value by two-tailed t test. **G,** Biaxial plots of Ki-67 and GrB fluorescence staining intensity in
1135 TNFα- or TNFα+ CD8 T cells. **H,** Quantification of TNFα- and TNFα+ CD8 T cells as % of cells binned into
1136 high expression gates for each marker. P value by two-tailed t tests. n=5 mice from one representative experiment.
1137 Two independent experiments were performed. **I and J,** Quantification of mean volumes and area under curves
1138 (AUC) for LLC MSI-H tumors treated with IgG or ICIs, grown in wild-type C57BL/6J mice or *Tnf*-null mice.
1139 Adjusted p values by Mann-Whitney test. n=5-12 from two independent experiments. **K and L,** Quantification
1140 of mean volumes and area under curves (AUC) for LLC MSI-H tumors treated with IgG or ICIs, implanted in
1141 *Cd4-cre(WT) Tnf(fl/fl or fl/+)* control mice or *Cd4-cre(+/-) Tnf(fl/fl)* mice. Adjusted p values by Mann-Whitney
1142 test. n=10-14 mice from two independent experiments. For all applicable panels, error bars represent mean +/-
1143 SD.

1144

Figure 6

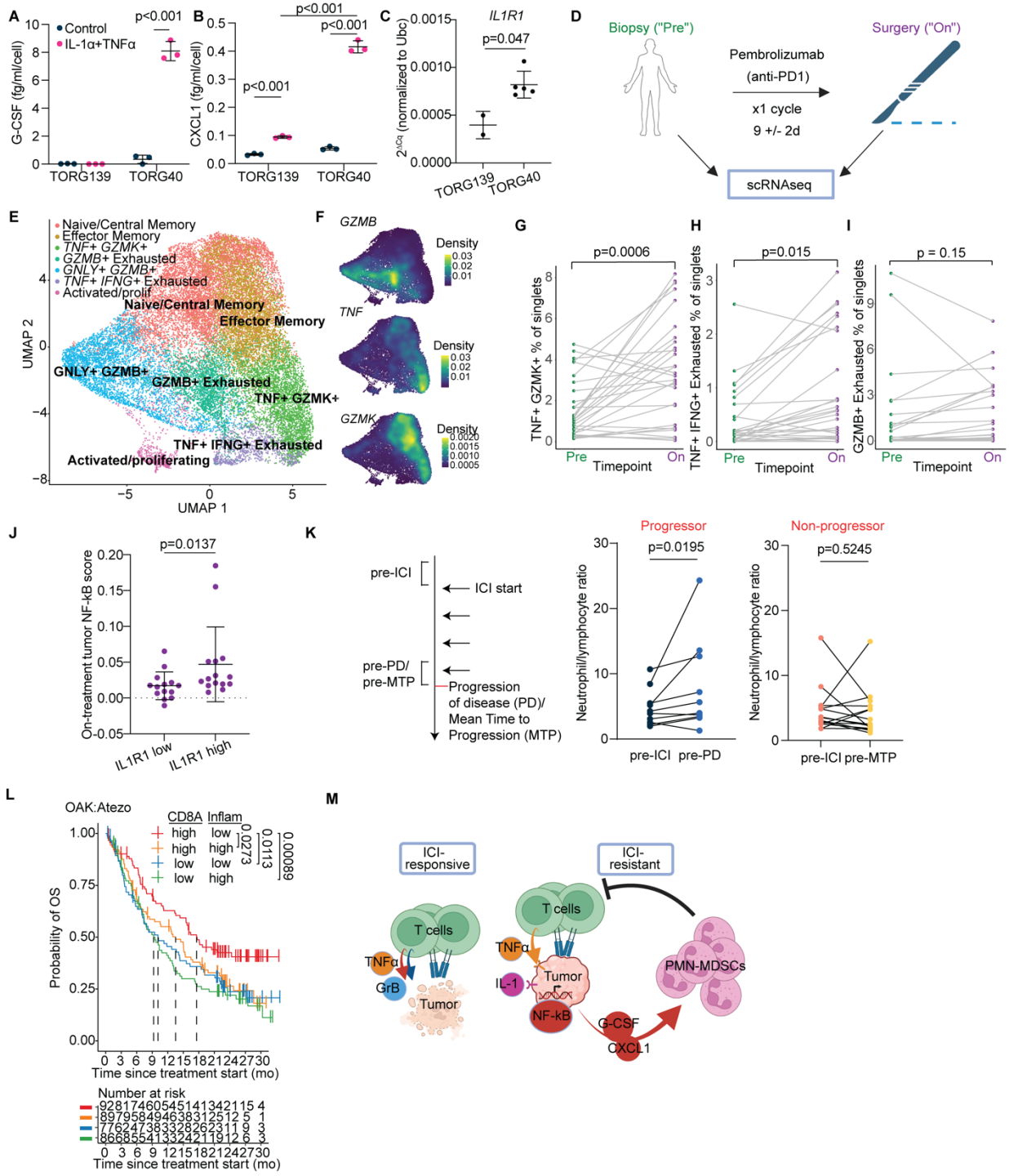

1145

1146 **Figure 6: T cell, tumor, and neutrophil inflammation circuit in human cancer.**

1147 **A,** ELISA quantification of G-CSF in supernatant of breast cancer organoid culture following indicated treatments
1148 for 24h, from one representative experiment with n=3 biological replicates. Two independent experiments were
1149 performed. P value by two-tailed t test. **B,** Analysis as in **(A)** for CXCL1. Adjusted p values by t tests. **C,** *IL1R1*
1150 transcript quantification by RT-qPCR for breast organoid models from two independent experiments. P value by
1151 one-tailed Mann-Whitney test. **D,** Schematic of the BIOKEY study (EGAS00001004809) analyzed in **(E-J). E,**
1152 UMAP of 24,349 CD8 T cells color coded by CD8 T cell phenotype. **F,** UMAP cell density plots of *GZMB*, *TNF*,
1153 and *GZMK* expressing cells. **G-I,** Percent of cells in indicated cluster out of singlet cells in tumor for pre vs. on-
1154 treatment samples for each patient. P value by two-tailed Wilcoxon matched-pairs signed rank test. **J,**
1155 Quantification of on-treatment NF-κB scores in tumor cells for each patient, stratified by *IL1R1* expression in ≥1%
1156 (high) or <1% (low) of tumor cells. **K,** Definitional schema and plot of neutrophil/lymphocyte ratios in peripheral
1157 blood of patients with MSI-H tumors treated with ICI therapy, stratified by progression vs. non-progression status.
1158 P value by two-tailed Wilcoxon matched-pairs signed rank test. **L,** Kaplan-Meier curves of patients in the OAK
1159 trial (NCT02008227), stratified by *CD8A* status and inflammation gene score status ("inflam"). P values by log-
1160 rank test. **M,** Mechanistic model.